

# Quantum state preparation for multivariate functions

Matthias Rosenkranz<sup>1</sup>, Eric Brunner<sup>1</sup>, Gabriel Marin-Sanchez<sup>1</sup>, Nathan Fitzpatrick<sup>2</sup>, Silas Dilkes<sup>2</sup>, Yao Tang<sup>2</sup>, Yuta Kikuchi<sup>3,4</sup>, and Marcello Benedetti<sup>1</sup>

<sup>1</sup>Quantinuum, Partnership House, Carlisle Place, London SW1P 1BX, United Kingdom

<sup>2</sup>Quantinuum, Terrington House, 13-15 Hills Road, Cambridge CB2 1NL, United Kingdom

<sup>3</sup>Quantinuum K.K., Otemachi Financial City Grand Cube 3F, 1-9-2 Otemachi, Chiyoda-ku, Tokyo, Japan

<sup>4</sup>Interdisciplinary Theoretical and Mathematical Sciences Program (iTHEMS), RIKEN, Wako, Saitama 351-0198, Japan

31 May, 2024

A fundamental step of any quantum algorithm is the preparation of qubit registers in a suitable initial state. Often qubit registers represent a discretization of continuous variables and the initial state is defined by a multivariate function. We develop protocols for preparing quantum states whose amplitudes encode multivariate functions by linearly combining block-encodings of Fourier and Chebyshev basis functions. Without relying on arithmetic circuits, quantum Fourier transforms, or multivariate quantum signal processing, our algorithms are simpler and more effective than previous proposals. We analyze requirements both asymptotically and pragmatically in terms of near/medium-term resources. Numerically, we prepare bivariate Student's  $t$ -distributions, 2D Ricker wavelets and electron wavefunctions in a 3D Coulomb potential, which are initial states with potential applications in finance, physics and chemistry simulations. Finally, we prepare bivariate Gaussian distributions on the Quantinuum H2-1 trapped-ion quantum processor using 24 qubits and up to 237 two-qubit gates.

## 1 Introduction

State preparation is a computational problem that appears as a sub-routine in many quantum algorithms. In Hamiltonian simulation, we approximate the real-time evolution  $e^{-itH} |\psi\rangle$  of an initially prepared state  $|\psi\rangle$ . Quantum algorithms for linear systems of equations  $A|x\rangle = |b\rangle$  require the preparation of  $|b\rangle$  in the first place. Other examples are found in the literature of quantum algorithms for partial differential equations [1, 2], financial instrument pricing [3–5], quantum chemistry simulations [6–10], high-energy or nuclear physics [11–13], and other applications [14].

The computational complexity of state preparation is well understood [15–20] and it is connected to that

of synthesizing circuits for arbitrary unitary matrices. Algorithms for preparing generic  $n$ -qubit states incur an unavoidable exponential scaling, either in terms of circuit depth [21] or number of ancilla qubits [22]. Under certain assumptions, however, the scaling can be improved. For the special case of  $k$ -sparse states, i.e. states with  $k$  non-zero amplitudes, there exists an efficient preparation using  $\log(nk)$  circuit depth and  $\mathcal{O}(nk \log k)$  ancilla qubits [22]. For more structured states, such as when the amplitudes are defined by a function, there exist a number of efficient algorithms. For example, [23–26] consider certain classes of probability density functions; [27–29] consider real-valued functions approximated by polynomials; [30] considers complex-valued continuous functions. Quantum arithmetic circuits are among the most expensive components in state preparation algorithms. Recent work has aimed at limiting their use, potentially leading to a reduction of the number of qubits and gates. When the amplitudes are unknown and provided by a black-box, the use of arithmetic circuits can be limited to simple comparisons against some initial reference state [31–33], or replaced by linear combination of unitaries circuits [34]. When amplitudes are given by a known function instead, quantum signal processing (QSP) [35–39] can be used to avoid arithmetic circuits altogether [40].

In this work, we contribute to the state preparation problem by considering the case where the amplitudes are defined by multivariate functions. The multivariate case is seldom discussed in the literature and presents its unique challenges. For example, multivariate versions of QSP appear to be much more complicated and highly constrained [41–43]. We attack the multivariate state preparation problem using a simple set of primitives and without using arithmetic circuits. We make use of (i) function approximation by truncated Fourier or Chebyshev series, (ii) block-encoding of the corresponding basis functions, and (iii) linear combination of unitaries. The resources required by our algorithms depend on three hyperparameters: the number of dimensions  $D$ , the number of bits  $n$  used for the discretization of each dimension, and the degree  $d$  used for function approximation in

Matthias Rosenkranz: [matthias.rosenkranz@quantinuum.com](mailto:matthias.rosenkranz@quantinuum.com)

Marcello Benedetti: [marcello.benedetti@quantinuum.com](mailto:marcello.benedetti@quantinuum.com)

each dimension. We obtain a number of two-qubit gates that scales as  $\mathcal{O}(d^D + Dn \log d)$  for Fourier series and as  $\mathcal{O}(d^D + Ddn \log n)$  for Chebyshev series. The total number of qubits scales as  $\mathcal{O}(Dn + D \log d)$  for both methods.

For the special case of Fourier series approximation, the closest work to ours is the Fourier series loader (FSL) [44]. This method loads the Fourier coefficients in the main qubit register, hence avoiding the use of ancilla qubits. It then employs the quantum Fourier transform (QFT) to prepare the target state using additional  $\mathcal{O}(n^2)$  gates. Related ideas of using the QFT for Fourier series interpolation of a target function from a coarse grid to a finer grid were earlier explored in [45]. In comparison, our method uses ancilla qubits, but it is more general, and cuts down the number of two-qubit gates by avoiding QFT. A related method called the Walsh series loader (WSL) [46] approximates the target function by a Walsh series, which is loaded on the quantum computer using techniques from [47]. While WSL is shallower than FSL, it introduces a further approximation error which also affects the probability of success. Our method does not have this additional error.

## 2 Methods

We wish to prepare a quantum state with amplitudes proportional to a multivariate target function. We consider complex target functions,  $f: [-1, 1]^D \rightarrow \mathbb{C}$ . For simplicity of exposition, let us first discuss the one-dimensional case,  $D = 1$ . We assume that  $f$  has a Fourier or Chebyshev series representation of the form  $f(x) = \sum_{k=-\infty}^{\infty} \hat{c}_k e^{i\pi k x}$  or  $f(x) = \sum_{k=0}^{\infty} \hat{c}_k T_k(x)$ , respectively, with  $T_k(x)$  the  $k$ -th Chebyshev polynomial of the first kind. For the Fourier case, this requires the function to be periodic with period 2 on the whole interval  $[-1, 1]$ . However, we also work with non-periodic target functions as Fourier series by focusing on the interval  $[0, 1]$  and using the interval  $[-1, 0]$  for its periodic extension (see Appendix B).

Next, we approximate the target function with a finite Fourier or Chebyshev series of the form

$$f_d^F(x) = \sum_{k=-d}^d c_k e^{i\pi k x} \quad (\text{Fourier}) \quad (1)$$

and

$$f_d^C(x) = \sum_{k=0}^d c_k T_k(x) \quad (\text{Chebyshev}), \quad (2)$$

respectively. The largest index in the sum,  $d$ , is the *degree* of the polynomial (for which  $c_d$  or  $c_{-d}$  does not vanish). We use  $f_d$  to indicate either  $f_d^F$  or  $f_d^C$ , which should be clear from context. If the coefficients of the infinite series are known, one approximation is truncation by setting  $c_k = \hat{c}_k$  for all  $|k| \leq d$ . Another

approximation is interpolation such that  $f_d$  matches  $f$  in a number of interpolation points. Computing accurate coefficients for this interpolant can be done with the fast Fourier transform (FFT) with classical preprocessing cost  $\mathcal{O}(d \log d)$  (see Appendix A–B). A rule-of-thumb is that the smoother the target function the faster its finite series approximations converges with increasing  $d$  [48, 49].

For the multivariate case, we consider approximations with products of the corresponding basis functions. For example, in two dimensions

$$f_{d_x, d_y}^F(x, y) = \sum_{k=-d_x}^{d_x} \sum_{l=-d_y}^{d_y} c_{k,l} e^{i\pi k x} e^{i\pi l y} \quad (\text{Fourier}) \quad (3)$$

and

$$f_{d_x, d_y}^C(x, y) = \sum_{k=0}^{d_x} \sum_{l=0}^{d_y} c_{k,l} T_k(x) T_l(y) \quad (\text{Chebyshev}). \quad (4)$$

This generalizes to  $D$  dimensions with degrees  $\mathbf{d} = (d_1, d_2, \dots, d_D)$ . The following protocols prepare a quantum state  $\sum_{\mathbf{x}} g_{\mathbf{d}}(\mathbf{x}) |\mathbf{x}\rangle$  with  $g_{\mathbf{d}}(\mathbf{x}) = f_{\mathbf{d}}(\mathbf{x}) / \sqrt{\sum_{\mathbf{x}} |f_{\mathbf{d}}(\mathbf{x})|^2}$  for all  $\mathbf{x}$  on a grid of size  $2^{n_1} \times 2^{n_2} \times \dots \times 2^{n_D}$ .

### 2.1 Discretization

In this work, each variable is assigned to its own ‘main’ register. We use the notation  $x$  for the variable and  $n_x$  for the number of qubits in the register. The variable is therefore discretized on a grid of  $2^{n_x}$  points. In the univariate setting, we simplify the notation to  $n = n_x$ .

Recall that when working with Fourier series approximations, we focus on the non-negative part of the domain,  $x \in [0, 1]$ . In this case the uniform grid of points is represented by the  $n$ -qubit diagonal matrix

$$H^F = \frac{1}{2^n - 1} \begin{pmatrix} 0 & & & \\ & 1 & & \\ & & \ddots & \\ & & & 2^n - 1 \end{pmatrix}. \quad (5)$$

For example, with  $n = 2$  we have grid points  $0, \frac{1}{3}, \frac{2}{3}, 1$ .

When working with Chebyshev series approximations we don’t need periodic extensions. Thus we use the negative part of the domain as well,  $x \in [-1, 1]$ . The uniform grid of point is then represented by the  $n$ -qubit diagonal matrix

$$H^C = 2H^F - I^{\otimes n}, \quad (6)$$

where  $I = \begin{pmatrix} 1 & 0 \\ 0 & 1 \end{pmatrix}$  is the identity matrix. For example, with  $n = 2$  we have grid points  $-1, -\frac{1}{3}, \frac{1}{3}, 1$ .

It is important to note that this grid is uniform and should not be confused with the grid of Chebyshev nodes commonly used in polynomial interpolation.

In the following we often use  $H$  to indicate either  $H^F$  or  $H^C$ , which should be clear from the context. Note that both matrices (5) and (6) have the operator norm  $\|H\| = 1$ . Grids for multivariate functions are built by taking tensor products  $H \otimes \dots \otimes H$ , and this does not change the operator norm.

## 2.2 Block-encoding

To construct the Fourier and Chebyshev approximations we shall block-encode the corresponding basis functions. We begin with the standard definition of block-encoding. An  $(n + m)$ -qubit unitary  $W_L$  is an  $(\lambda, m, \epsilon)$ -block-encoding of  $L \in \mathbb{C}^{2^n \times 2^n}$  if

$$\left\| L - \lambda \left( \langle 0|^{\otimes m} \otimes I^{\otimes n} \right) W_L \left( |0\rangle^{\otimes m} \otimes I^{\otimes n} \right) \right\| \leq \epsilon, \quad (7)$$

where  $m$  is the number of ancilla qubits,  $\lambda$  is a normalization constant such that  $\lambda \geq \|L\| - \epsilon$  and  $\epsilon$  is the error.

We make use of the linear combination of unitaries (LCU) [50] to construct block-encoding circuits. Assume the input matrix is given as a weighted sum of  $K$  unitary operators  $\{U_k\}_k$ , i.e.  $L = \sum_{k=0}^{K-1} \lambda_k U_k$ . To deal with negative and complex coefficients, we write them in polar form,  $\lambda_k = e^{i\gamma_k} |\lambda_k|$ , and compute the normalization  $\lambda = \sum_{k=0}^{K-1} |\lambda_k|$ . LCU uses  $m = \lceil \log_2 K \rceil$  ancilla qubits and the following unitary operators

$$A = \sum_{k=0}^{K-1} \sqrt{\frac{|\lambda_k|}{\lambda}} |k\rangle\langle 0|^{\otimes m} \otimes I^{\otimes n} + \text{u.c.}, \quad (8)$$

$$B = \sum_{k=0}^{K-1} |k\rangle\langle k| \otimes U_k, \quad (9)$$

$$C = \sum_{k=0}^{K-1} e^{i\gamma_k} |k\rangle\langle k| \otimes I^{\otimes n}, \quad (10)$$

where u.c. stands for unitary completion. With these definitions, the operator  $A^\dagger C B A$  yields

$$\left( \langle 0|^{\otimes m} \otimes I^{\otimes n} \right) A^\dagger C B A \left( |0\rangle^{\otimes m} \otimes I^{\otimes n} \right) = \frac{1}{\lambda} \sum_{k=0}^{K-1} \lambda_k U_k, \quad (11)$$

which is a  $(\lambda, m, 0)$ -block-encoding of  $L$ .

Let us discuss the important special case where  $U_k = U^k$  are powers of some unitary  $U$ . When  $k \geq 0$  is encoded to the state as a binary string  $|k\rangle = |k_{m-1}\rangle \otimes \dots \otimes |k_0\rangle$ , corresponding to the binary representation  $k = 2^0 k_0 + 2^1 k_1 + \dots + 2^{m-1} k_{m-1}$ , the

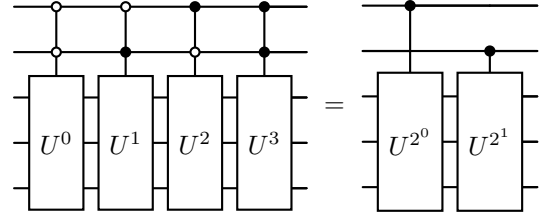


Figure 1: Circuit identity Eq. (12) for  $\sum_k |k\rangle\langle k| \otimes U^k$  with  $K = 4$  and  $m = 2$ .

$B$  operator in Eq. (9) takes the form

$$\sum_{k=0}^{K-1} |k\rangle\langle k| \otimes U^k = \prod_{i=0}^{m-1} \left[ |0\rangle\langle 0|_i \otimes I^{\otimes n} + |1\rangle\langle 1|_i \otimes U^{2^i} \right] \quad (12)$$

where we highlight the relevant qubits with a subscript and assume identity gates on all other qubits. This simple identity is illustrated in Fig. 1. It significantly reduces the resources required for LCU in our use case.

Note that the approximate functions we wish to encode, Eqs. (1) and (2), are weighted sums of basis functions. In the following sections we implement the  $k$ -th basis functions as the operator  $U_k$  and then use LCU to block-encode the whole weighted sum. The circuit construction for the operators  $A$  and  $C$  does not change depending on whether the Fourier or Chebyshev basis is used, while the circuit construction for the operator  $B$  does.

## 2.3 Fourier basis functions

We seek a circuit construction for the Fourier basis  $B$  operator  $B^F = \sum_{k=0}^{K-1} |k\rangle\langle k| \otimes U_k$  with  $U_k$  a block-encoding of the  $k$ -th Fourier basis function. As the univariate Fourier basis in Eq. (1) is defined as  $\{e^{i\pi k' x}\}_{k'=-d}^d$ , the  $k'$ -th Fourier basis function applied to  $H^F$  is the real-time evolution operator  $U_{k'} = U^{k'} = e^{i\pi k' H^F}$ . By the definition in Eq. (7), a unitary operator is a trivial  $(1, 0, 0)$ -block-encoding of itself. However, we need to show that there exists an efficient circuit to implement the operator for any value of  $k'$ . It can be verified by inspection that

$$e^{i\pi k' H^F} = \bigotimes_{j=0}^{n-1} P_j \left( \frac{\pi k' 2^j}{2^n - 1} \right), \quad (13)$$

where

$$P(\theta) = \begin{pmatrix} 1 & 0 \\ 0 & e^{i\theta} \end{pmatrix}, \quad (14)$$

is the phase shift gate and subscript  $j$  indicates application of the gate to the  $j$ -th qubit. This is a block-encoding circuit for any Fourier basis function and uses only  $n$  single-qubit phase shift gates.

To map this block-encoding to the special case discussed at the end of Sec. 2.2, we first write

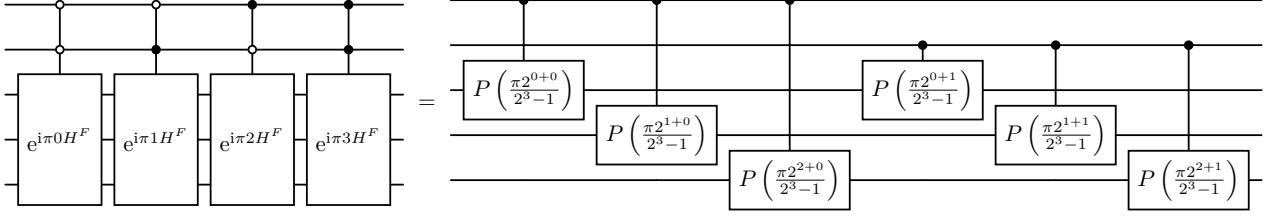


Figure 2: Example of circuit synthesis for the Fourier basis with Hamiltonian  $H^F$ ,  $a = 2$  ancilla and  $n = 3$  main qubits. The special structure of this Hamiltonian leads to an efficient circuit made of  $a \times n$  controlled-phase gates.

$U_k = U^{-d} U^k$  with  $k = 0, 1, \dots, 2d$ . Next we implement the operator  $\sum_{k=0}^{K-1} |k\rangle\langle k| \otimes e^{i\pi k H^F}$  using Eq. (12) with  $U = e^{i\pi H^F}$  and an ancilla register of size  $m = a = \log_2(2d + 1)$ , and synthesize the circuit efficiently as

$$\sum_{k=0}^{K-1} |k\rangle\langle k| \otimes e^{i\pi k H^F} = \prod_{i=0}^{a-1} \prod_{j=0}^{n-1} \left[ |0\rangle\langle 0|_i \otimes I_j + |1\rangle\langle 1|_i \otimes P_j \left( \frac{\pi 2^{j+i}}{2^n - 1} \right) \right]. \quad (15)$$

This can be verified using the factorization  $e^{i\pi k H^F} = \prod_{i=0}^{a-1} e^{i\pi k_i 2^i H^F}$ , followed by Eq. (13), and using  $P_j(0) = I_j$ . An example circuit diagram is provided in Fig. 2. Finally, we construct

$$B^F = U^{-d} \sum_{k=0}^{K-1} |k\rangle\langle k| \otimes e^{i\pi k H^F} \quad (16)$$

by applying the circuit Eq. (15) followed by the circuit for  $U^{-d}$  using Eq. (13) one more time. We have thus obtained a controlled  $(1, 0, 0)$ -block-encoding circuit for the Fourier basis functions. It requires only  $a \times n$  controlled-phase gates and additional  $n$  single-qubit gates from the circuit for  $U^{-d}$ . A controlled-phase gate can be implemented with two controlled-not (CX) gates plus single-qubit gates.

## 2.4 Chebyshev basis functions

We seek a circuit construction for the Chebyshev basis  $B$  operator  $B^C = \sum_{k=0}^{K-1} |k\rangle\langle k| \otimes U_k$  with  $U_k$  a block-encoding of the  $k$ -th Chebyshev polynomial. As the univariate Chebyshev basis in Eq. (2) is defined as  $\{T_k(x) = \cos(k \cos^{-1}(x))\}_{k=0}^d$ , the  $k$ -th Chebyshev basis function applied to  $H^C$  is not a unitary operator. We proceed by first block-encoding  $H^C$ , and then using the algebra of block-encoding circuits to obtain  $T_k(H^C)$ .

Using Eqs. (5) and (6), we obtain

$$H^C = \sum_{j=0}^{n-1} \left( -\frac{2^j}{2^n - 1} \right) Z_j = \sum_{j=0}^{n-1} \left( \frac{2^j}{2^n - 1} \right) X_j Z_j X_j. \quad (17)$$

Here  $Z_j$  and  $X_j$  indicate the Pauli operators  $Z = \begin{pmatrix} 1 & 0 \\ 0 & -1 \end{pmatrix}$  and  $X = \begin{pmatrix} 0 & 1 \\ 1 & 0 \end{pmatrix}$  applied to the  $j$ -th qubit, respectively. The result is a linear combination of  $n$  unitaries with which we can define a  $(1, b, 0)$ -block-encoding of  $H^C$ ,  $V = A_V^\dagger C_V B_V A_V$ , where  $C_V = I$  and

$$A_V = \sum_{j=0}^{n-1} \sqrt{\frac{2^j}{2^n - 1}} |j\rangle\langle 0|^{\otimes m} \otimes I^{\otimes n} + \text{u.c.}, \quad (18)$$

$$B_V = \sum_{j=0}^{n-1} |j\rangle\langle j| \otimes X_j Z_j X_j. \quad (19)$$

Such a block-encoding requires  $m = b = \lceil \log_2 n \rceil$  ancilla qubits.

Next, Lemma 8 in Ref. [51] shows that a block-encoding  $V$  can be used to derive another block-encoding  $U_V$  that satisfies the qubitization condition

$$U_V = \bigoplus_{\xi} \begin{pmatrix} \xi & -\sqrt{1 - \xi^2} \\ \sqrt{1 - \xi^2} & \xi \end{pmatrix}_{\xi}, \quad (20)$$

where  $\xi$ 's are the eigenvalues of the block-encoded matrix and each term is represented in the basis  $\{|G_{\xi}\rangle, |G_{\xi}^{\perp}\rangle\}$  defined in Ref. [51]. Moreover, Corollary 9 in Ref. [51] shows that in the special case where  $V^2 = I$  (which holds true here given that  $B_V^2 = I$  and  $C_V = I$ ) the qubitized block-encoding takes a simple form

$$U_V = \left( (2|0\rangle\langle 0|^{\otimes b} - I^{\otimes b}) \otimes I^{\otimes n} \right) V. \quad (21)$$

We now combine two results from the literature. The first result is Lemma 16 in Ref. [52]. It states that for positive integer  $k$

$$\left( \begin{pmatrix} \xi & -\sqrt{1 - \xi^2} \\ \sqrt{1 - \xi^2} & \xi \end{pmatrix} \right)^k = \begin{pmatrix} T_k(\xi) & -\sqrt{1 - \xi^2} u_{k-1}(\xi) \\ \sqrt{1 - \xi^2} u_{k-1}(\xi) & T_k(\xi) \end{pmatrix}, \quad (22)$$

where  $u_k$  are Chebyshev polynomials of the second kind. For  $k = 0$  we define the above expression as the identity matrix. The second result we use is Lemma 54 in Ref. [36] which deals with products of

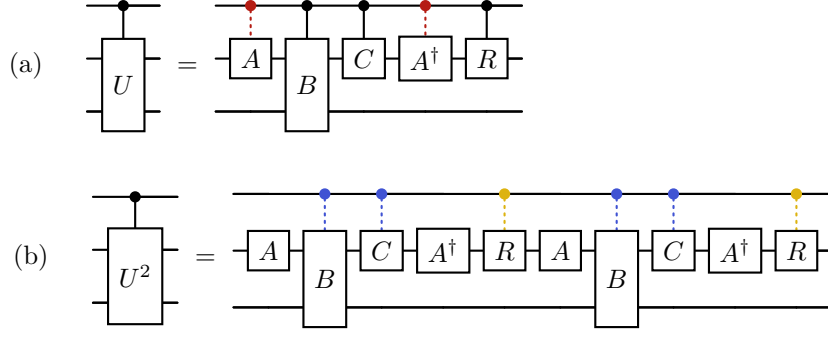


Figure 3: Simplifications used in the block-encoding circuit of Chebyshev basis functions. (a) For controlled- $U$ , where  $U$  is any LCU circuit, one can remove the controls depicted in red. (b) For the specific case where  $B^2 = I$  and  $C^2 = I$  it is possible to simplify controlled- $U^2$  as well. One can remove either the blue or the yellow colored controls, depending on which option is more convenient. Our method uses controlled- $U^{2^i}$  and thus benefits significantly from these techniques.

block-encodings. In the case where the encoded matrices are unitaries and their normalization constant is  $\lambda = 1$ , the product of  $(1, b, 0)$ -block-encodings yields the  $(1, b, 0)$ -block-encoding of the product. Moreover, since  $U_V$  is the direct sum in Eq. (20), powers of  $U_V$  preserve the qubitization condition. It follows that

$$U_V^k = \bigoplus_{\xi} \begin{pmatrix} T_k(\xi) & -\sqrt{1-\xi^2} u_{k-1}(\xi) \\ \sqrt{1-\xi^2} u_{k-1}(\xi) & T_k(\xi) \end{pmatrix}_{\xi}, \quad (23)$$

and  $U_V^0 = I$ . This is a  $(1, b, 0)$ -block-encoding of the  $k$ -th Chebyshev polynomial applied to  $H^C$ , i.e.  $T_k(H^C) = (\langle 0|^{\otimes b} \otimes I^{\otimes n}) U_V^k (|0\rangle^{\otimes b} \otimes I^{\otimes n})$ . Note that the algebra of qubitized block-encodings is also used in Ref. [53] to implement Krylov basis vectors and Lanczos' method on a quantum computer. We emphasize that our method works because  $\lambda = \|H^C\| = 1$ . For  $\lambda \neq 1$  we would not obtain the correct result after rescaling the eigenvalues of  $H$  since  $T_k(H/\lambda) \neq T_k(H)/\lambda$  (but see Section 5.1 of Ref. [54] for approximate solutions when this issue arises).

To construct the finite Chebyshev series Eq. (2) from the block-encoding circuit  $U_V^k$  we insert  $U_V^k$  into Eq. (9). To implement  $U_V^k$  controlled on the value of  $k$  we again use the identity in Eq. (12) with  $m = a$  and obtain

$$\begin{aligned} B^C &= \sum_{k=0}^{K-1} |k\rangle\langle k| \otimes U_V^k \\ &= \prod_{i=0}^{a-1} \left[ |0\rangle\langle 0|_i \otimes I^{\otimes n+b} + |1\rangle\langle 1|_i \otimes U_V^{2^i} \right]. \end{aligned} \quad (24)$$

We can save some resources when controlling  $U_V$ . First, we can remove the control on  $A_V$  and  $A_V^\dagger$  since they cancel when no operation is performed in between. Second, when controlling  $U_V^2$ , we can either remove the control on  $B_V$  or on  $R = 2|0\rangle\langle 0|^{\otimes b} - I^{\otimes b}$ . These improvements are shown in the circuit diagrams in Fig. 3 and for our purposes we remove the control on  $B_V$ .

To provide a gate count for  $B^C$  in Eq. (24), we start with a gate count for  $|1\rangle\langle 1|_i \otimes U_V^2$  recalling  $U_V = R A_V^\dagger C_V B_V A_V$ . The operators  $A_V$  and  $A_V^\dagger$  in  $U_V^2$  can be implemented with a  $b$ -qubit state preparation circuit with real coefficients, requiring  $2^b$  CX gates each [17].  $B_V$  costs  $n$   $b$ -qubit controlled  $Z$  gates, which we denote as  $C^b Z$ . Controlled  $R$  costs one  $C^b Z$  gate. In total  $|1\rangle\langle 1|_i \otimes U_V^2$  costs  $2(n+1)$   $C^b Z$  gates and  $2 \cdot 2^b$  CX gates. For Eq. (24) we need to implement  $2^{i-1}$  copies of  $|1\rangle\langle 1|_i \otimes U_V^2$ . By summing up the gate counts for each copy we get the following totals for  $B^C$ :  $\sum_{i=0}^{a-1} 2^i (n+1) = (2^a - 1)(n+1)$   $C^b Z$  gates and  $\sum_{i=0}^{a-1} 2^i \cdot 2^b = (2^a - 1)2^b$  CX gates.

We wish to reduce gate counts to two-qubit gates only. Each  $C^b Z$  gate can be implemented with  $\mathcal{O}(b)$  gates [55], giving a total for  $B^C$  of  $\mathcal{O}[(2^a - 1)((n+1)b + 2^b)] = \mathcal{O}(2^a n b)$  CX gates. Here we kept only dominant terms in  $d$  and  $n$ .

## 2.5 State preparation in 1 and 2 dimensions

We now utilize our building-blocks for the construction of quantum states defined by truncated series expansions. In this section we drop the superscripts  $F$  for Fourier and  $C$  for Chebyshev, since the protocols are almost identical. Then, the  $n$ -qubit discretization of the domain ( $2^n$  points) is denoted as  $H$ , and the block-encoding of the  $k$ -th basis function is denoted as  $U_k$ .

We begin with one-dimensional functions  $f$  approximated by either Eq. (1) or Eq. (2), here both denoted by  $f_d$ . Without further assumptions, the number of terms is  $K = 2d + 1$  for Fourier series and  $K = d + 1$  for Chebyshev series. Each basis function is associated to a complex coefficient  $c_k$  which we rewrite as  $c_k = e^{i\phi_k} |c_k|$ . Then

$$f_d(H) = \sum_{k=0}^{K-1} c_k U^k = \mathcal{N} \sum_k e^{i\phi_k} \frac{|c_k|}{\mathcal{N}} U^k, \quad (25)$$

where we normalize the coefficients with  $\mathcal{N} = \sum_k |c_k|$ . We encode the coefficients using operators  $A$  and  $C$



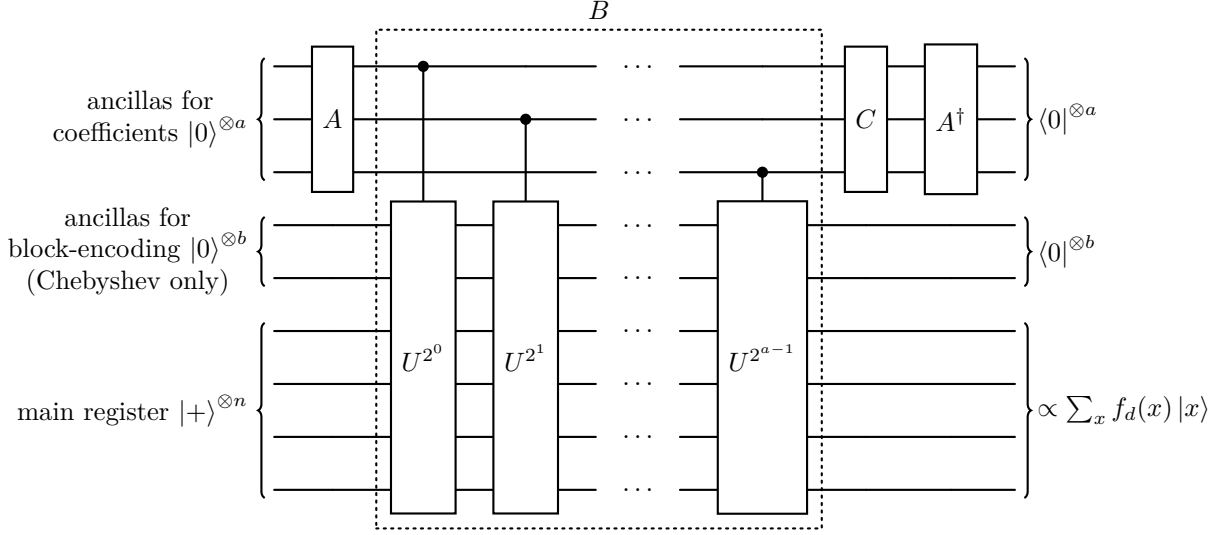


Figure 4: Quantum circuit for state preparation in one dimension. The amplitudes are defined by a finite series, such as Fourier or Chebyshev. Circuit  $U$  is the block-encoding of the corresponding basis functions and may require  $b$  additional ancilla qubits. Each bit in the coefficient register drives the application of powers of the block-encoding circuit. For example, in the subspace where the coefficient ancillas are in state  $|k\rangle$ , we apply  $U^k$  to the other two registers. The algorithm succeeds if we measure the zero state on all  $a + b$  ancilla qubits.

(Eqs. (8) and (10)), and an ancilla register of size  $a = \lceil \log_2 K \rceil$ . We then use the operator  $B$  defined in Eq. (16) for Fourier and Eq. (24) for Chebyshev noting, however, that the Chebyshev method requires additional  $b$  ancilla qubits. We thus obtain a  $(\mathcal{N}, a + b, 0)$ -block-encoding  $A^\dagger CBA$  with

$$\left( \langle 0|^{\otimes(a+b)} \otimes I^{\otimes n} \right) A^\dagger CBA \left( |0\rangle^{\otimes(a+b)} \otimes I^{\otimes n} \right) = \frac{1}{\mathcal{N}} f_d(H). \quad (26)$$

We apply  $A^\dagger CBA$  to  $|0\rangle^{\otimes(a+b)} \otimes |+ \rangle^{\otimes n}$  with the uniform superposition  $|+ \rangle^{\otimes n} = \frac{1}{\sqrt{2^n}} \sum_x |x\rangle$  on the main register. Upon measuring the zero state for all the ancilla qubits, the protocol generates the unnormalized state  $\frac{1}{\mathcal{N}\sqrt{2^n}} \sum_x f_d(x) |x\rangle$ . The probability of success is given by  $p_{\text{success}} = \frac{\sum_x |f_d(x)|^2}{\mathcal{N}^2 2^n}$ . Renormalizing the

state (dividing by  $\sqrt{p_{\text{success}}}$ ) we obtain the desired result  $\sum_x g_d(x) |x\rangle := \frac{1}{\sqrt{\sum_x |f_d(x)|^2}} \sum_x f_d(x) |x\rangle$ . The full circuit is sketched in Fig. 4.

With the one-dimensional warm up, we have all the elements to construct states defined by bivariate functions  $f(x, y)$ . Again we start by discretizing the variables using  $n_x$  and  $n_y$  qubits in the main registers, which gives us a two-dimensional grid of  $2^{n_x} \times 2^{n_y}$  points. We then approximate  $f$  as a finite series of degrees  $d_x$  and  $d_y$ . The coefficients are rewritten as  $c_{k,l} = e^{i\phi_{k,l}} |c_{k,l}|$  where  $k = 0, \dots, K_x - 1$  and  $l = 0, \dots, K_y - 1$ , and  $K_x, K_y$  depend on the series type and degree as before. The normalization constant becomes  $\mathcal{N} = \sum_k \sum_l |c_{k,l}|$ . The LCU operators are now defined as:

$$A = \sum_{k=0}^{K_x-1} \sum_{l=0}^{K_y-1} \sqrt{\frac{|c_{k,l}|}{\mathcal{N}}} |k\rangle\langle 0|^{\otimes a_x} \otimes |l\rangle\langle 0|^{\otimes a_y} \otimes I^{\otimes(b_x+b_y+n_x+n_y)} + \text{u.c.}, \quad (27)$$

$$B_X = \sum_{k=0}^{K_x-1} |k\rangle\langle k| \otimes I^{\otimes a_y} \otimes U^k \otimes I^{\otimes(b_y+n_y)}, \quad (28)$$

$$B_Y = \sum_{l=0}^{K_y-1} I^{\otimes a_x} \otimes |l\rangle\langle l| \otimes I^{\otimes(b_x+n_x)} \otimes U^l, \quad (29)$$

$$C = \sum_{k=0}^{K_x-1} \sum_{l=0}^{K_y-1} e^{i\phi_{k,l}} |k\rangle\langle k| \otimes |l\rangle\langle l| \otimes I^{\otimes(b_x+b_y+n_x+n_y)}. \quad (30)$$

Applying the circuit to the uniform superposition of both main registers and post-selecting on the zero state of

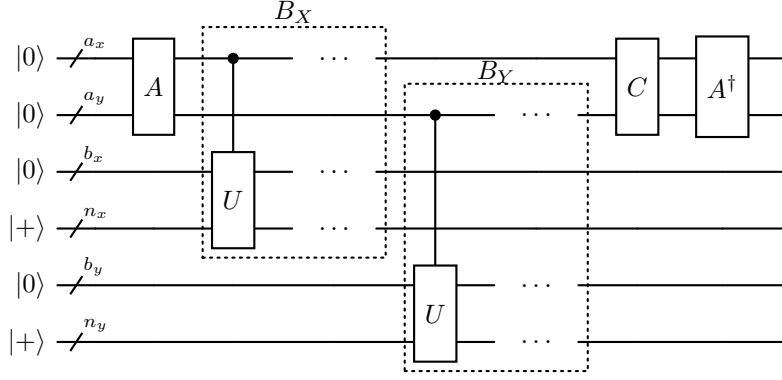


Figure 5: Quantum circuit for state preparation in two dimensions.

all the ancillas yields the desired state

$$\left( \langle 0|^{\otimes(a_x+a_y+b_x+b_y)} \otimes I^{\otimes(n_x+n_y)} \right) A^\dagger C B_Y B_X A \left( |0\rangle^{\otimes(a_x+a_y+b_x+b_y)} \otimes |+\rangle^{\otimes(n_x+n_y)} \right) = \frac{1}{\mathcal{N}\sqrt{2^{n_x+n_y}}} \sum_x \sum_y f_d(x, y) |x\rangle \otimes |y\rangle. \quad (31)$$

The protocol succeeds with probability

$$p_{\text{success}} = \frac{\sum_x \sum_y |f_d(x, y)|^2}{\mathcal{N}^2 2^{n_x+n_y}}. \quad (32)$$

To obtain the desired result we renormalize Eq. (31) by dividing by  $\sqrt{p_{\text{success}}}$ . The full circuit for bivariate state preparation is sketched in Fig. 5. The generalization of this protocol to arbitrary number of variables is straightforward.

## 2.6 Resource scaling for state preparation in arbitrary dimension

We can extrapolate the resource costs given in the previous sections for the one-dimensional case to estimate the scaling of state preparation in arbitrary dimensions. We focus on the number of qubits and CX gate count as a proxy for the two-qubit gate count, which is the main resource cost for our algorithm on near-term hardware. We neglect single-qubit gates.

Let us recall the resource requirements for state preparation with one variable ( $D = 1$ ). The operator  $B$  costs  $\mathcal{O}(an)$  CX gates for the Fourier approach (Sec. 2.3) and  $\mathcal{O}(2^a nb)$  CX gates for the Chebyshev approach (Sec. 2.4). The size of the ancilla register  $a$  is determined by the number of coefficients in the approximating series  $f_d$ , namely,  $a = \lceil \log_2(2d+1) \rceil$  for Fourier series and  $a = \lceil \log_2(d+1) \rceil$  for Chebyshev series. The block-encodings of the Chebyshev basis functions require an additional ancilla register of size  $b = \lceil \log_2 n \rceil$ .  $A$ ,  $A^\dagger$ , Eq. (8), and  $C$ , Eq. (10), can be implemented with  $a$ -qubit circuits requiring  $\mathcal{O}(2^a)$  CX gates each.

We now provide the resource requirements for state preparation in arbitrary dimension. First, we assume

that there are  $D$  variables, each discretized with  $n$  qubits, i.e. a total of  $Dn$  qubits in the main registers. Second, we assume the same degree  $d$  for each variable. The coefficients are encoded in ancilla registers  $a_1, a_2, \dots, a_D$  each with size  $a$ . Then the total number of ancilla qubits is  $Da = D\lceil \log_2(2d+1) \rceil$  and  $D(a+b) = D(\lceil \log_2(d+1) \rceil + \lceil \log_2 n \rceil)$  for the Fourier and Chebyshev approaches, respectively, where we inserted the respective expressions from the 1D case for  $a$  and  $b$ . The qubit counts are summarized in Table 1.

In general, the coefficients in a multivariate approximation  $f_d$  may take arbitrary values. Then the operators  $A$ ,  $A^\dagger$  and  $C$  can be implemented with  $Da$ -qubit circuits requiring  $\mathcal{O}(2^{Da})$  CX gates each. We have  $D$  operators  $B_1, B_2, \dots, B_D$ . Each  $B_i$  is controlled only on the corresponding coefficient ancilla register  $a_i$  and acts only on the corresponding main register  $n_i$ . For the Chebyshev case each  $B_i$  also acts on the corresponding block-encoding ancilla register  $b_i$ , cf. Fig. 5. Hence, implementing all  $B_i$  is  $D$  times the 1D implementation cost of  $B$ :  $\mathcal{O}(Dan)$  CX gates for the Fourier approach and  $\mathcal{O}(D2^a nb)$  CX gates for the Chebyshev approach. Summing the costs for  $A$ ,  $A^\dagger$ ,  $C$  and all  $B_i$  and inserting the values for  $a$  and  $b$  yields  $\mathcal{O}(2^{D\lceil \log_2(2d+1) \rceil} + Dn\lceil \log_2(2d+1) \rceil)$  CX gates for the Fourier approach and  $\mathcal{O}(2^{D\lceil \log_2(d+1) \rceil} + Dn\lceil \log_2 n \rceil 2^{\lceil \log_2(d+1) \rceil})$  CX gates for the Chebyshev approach. The simplified expressions  $\mathcal{O}(d^D + Dn \log d)$  and  $\mathcal{O}(d^D + Ddn \log n)$ , respectively, are provided as the two-qubit gate count in Table 1.

Some remarks are in order. First, if we wanted to boost the probability of success to unity we could use amplitude estimation. That would increase the num-

|                         | Fourier   | Chebyshev  |
|-------------------------|---|--|
| Target function         | $[0, 1]^D \rightarrow \mathbb{C}$                                       | $[-1, 1]^D \rightarrow \mathbb{C}$                               |
| Classical preprocessing | Cost of computing coefficients, e.g. $\mathcal{O}(Dd^D \log d)$ for FFT |  |
| Main qubits             | $Dn$  | $Dn$   |
| Ancilla qubits          | $D \lceil \log_2(2d+1) \rceil$  | $D \lceil \log_2(d+1) \rceil + D \lceil \log_2 n \rceil$         |
| Two-qubit gates         | $\mathcal{O}(d^D + Dn \log d)$  | $\mathcal{O}(d^D + Ddn \log n)$                                  |
| Success probability     | $\mathcal{N}^{-2} 2^{-Dn} \sum_{\mathbf{x}}  f_d(\mathbf{x}) ^2$        | $\mathcal{N}^{-2} 2^{-Dn} \sum_{\mathbf{x}}  f_d(\mathbf{x}) ^2$ |

Table 1: Resources of our algorithm for preparing a quantum state with amplitudes proportional to a  $D$ -dimensional function represented on an equidistant grid of total size  $2^{Dn}$ . The method uses a Fourier or Chebyshev polynomial approximation  $f_d$  with maximal degree  $d$  in each dimension.  $\mathcal{N} = \sum_{\mathbf{k}} |c_{\mathbf{k}}|$  is a normalization dependent on the expansion coefficients  $c_{\mathbf{k}}$ .

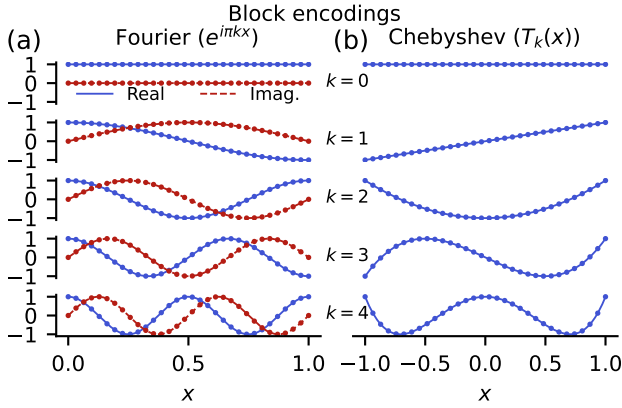


Figure 6: Block-encodings of the Fourier and Chebyshev basis functions. Markers are the diagonal of the Fourier block encoding, Eq. (13) in (a), and  $(|0\rangle^{\otimes b} \otimes I^{\otimes n}) U^k (|0\rangle^{\otimes b} \otimes I^{\otimes n})$  with Chebyshev block encoding  $U^k$ , Eq. (23) in (b), for  $n = 5$  qubits (32 grid points). Lines are the corresponding continuous basis functions  $e^{i\pi k x}$  and  $T_k(x)$ .

ber of gates by a multiplicative factor of  $\mathcal{O}(p_{\text{success}}^{-1/2})$ . Second, the degree  $d$  for each dimension must be chosen depending on the desired accuracy  $\varepsilon$ . The scaling of  $d(\varepsilon)$  is problem-dependent and not analyzed in this work. However, the protocol is efficient only if  $d \in \mathcal{O}(\text{poly}(n))$ , which limits the accuracy that can be achieved in general.

### 3 Results

With our first numerical simulations we visually inspect the block-encodings of Fourier and Chebyshev basis functions. In Fig. 6(a) we plot the diagonal of Eq. (13) for  $k = 0, \dots, 4$ . In Fig. 6(b) we show the diagonal of  $(|0\rangle^{\otimes b} \otimes I^{\otimes n}) U^k (|0\rangle^{\otimes b} \otimes I^{\otimes n})$  where  $U^k$  is given in Eq. (23). In both cases we use  $n = 5$ , leading to a  $x$ -axis discretization with 32 points. As expected the data points closely track  $e^{ik\pi H}$  in Fig. 6(a), and  $T_k(H)$  in Fig. 6(b).

#### 3.1 2D Ricker wavelet via Chebyshev series

To illustrate the Chebyshev approach, we consider a 2D Ricker wavelet centered at  $(0, 0)$ ,

$$f(x, y) = \frac{1}{\pi\sigma^4} \left( 1 - \frac{x^2 + y^2}{2\sigma^2} \right) e^{-\frac{x^2 + y^2}{2\sigma^2}}. \quad (33)$$

Wavelets of this form are used, e.g. in image or seismic data applications [56–58].

We interpolate the function on the domain  $[-1, 1]^2$  with the Chebyshev series Eq. (4) and compute its coefficients via the fast Fourier transform (see Appendix A). We choose the same degree and same grid size in each variable, i.e.  $d_x = d_y = d$  and  $n_x = n_y = n$ . Figure 7 shows results for approximating the 2D Ricker wavelet with  $\sigma = 0.5$  by a Chebyshev series of varying degree  $d$  and for different grid sizes  $2^n \times 2^n$ . Figure 7(a) illustrates the discretized target function and its absolute difference to the amplitudes of the prepared quantum state for degree  $d = 7$  and grid size  $2^4 \times 2^4$ . For this comparison we rescale the amplitudes from a noiseless simulation of the algorithm appropriately,

$$\tilde{g}_d(x, y) = g_d(x, y) \sqrt{\sum_{i=0}^{2^n-1} \sum_{j=0}^{2^n-1} |f(x_i, y_i)|^2}, \quad (34)$$

where  $x_i, y_i$  are the evaluated grid points. Figure 7(b) shows the maximum error  $\max_{(x,y)} |f(x, y) - \tilde{g}_d(x, y)|$  where the maximum is over grid points. Increasing the degree leads to rapid convergence of the amplitudes to the target function. We observe that the error between the rescaled amplitudes and the Chebyshev approximation  $f_d$  is at machine precision (not shown). Hence, the convergence of our method to the target function is determined by the convergence of the Chebyshev approximation. The grey line shows the maximum error of the Chebyshev approximation,  $\max_{(x,y) \in [-1,1]^2} |f(x, y) - f_d(x, y)|$ , evaluated numerically over the whole domain (not just the grid) via global optimization. The line is consistent with supergeometric convergence to the target function. The numerics are floored at machine



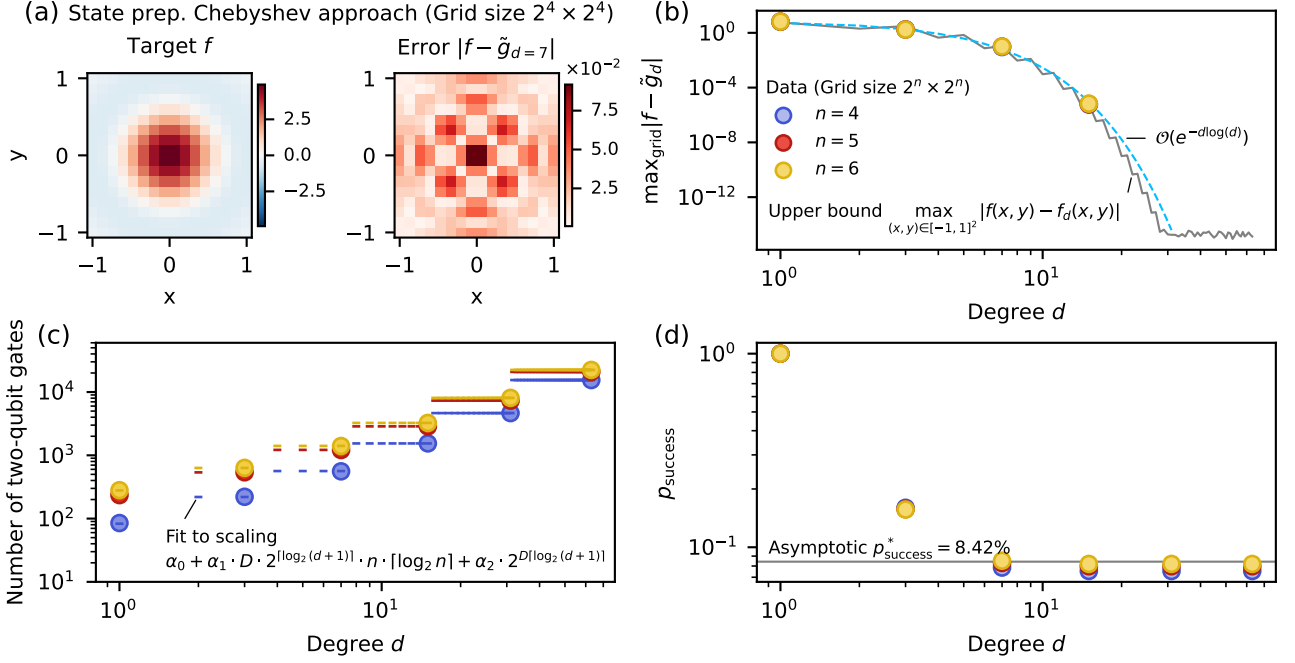


Figure 7: Resources for preparing an approximation to the 2D Ricker wavelet with products of Chebyshev polynomials of degree  $d$  in each dimension. (a) Discretized target function and the absolute difference to the rescaled amplitudes from a noiseless simulation of the algorithm for  $d = 7$ . (b) Maximum absolute error of the prepared state evaluated at the grid points for different grid sizes. The difference between the prepared state and the Chebyshev approximation is at machine precision (not shown). Hence, the maximum error of the noiseless simulation against the target function is upper bounded by the maximum error of the degree- $d$  Chebyshev interpolant over the (non-discretized) domain (grey line – floored at machine precision). The dashed line illustrates a super-exponential asymptotic error bound  $\mathcal{O}(e^{-d \log d})$ . (c) Two-qubit gate count for different grid sizes compiled with pytket optimization level 2 for the H2-1 default gate set. The line markers are a least-square fit of the data (round markers) to the worst-case scaling with  $\alpha_0 = -29.3, -47.3, -49.3$ ,  $\alpha_1 = 3.14, 4.47, 4.39$ ,  $\alpha_2 = 3.00, 3.00, 3.00$  for  $n = 4, 5, 6$  and  $D = 2$ . (d) Empirical (markers) and asymptotic success probability for  $n \rightarrow \infty$  and  $d \rightarrow \infty$  (line).

precision from around degree 30. The data from the algorithm’s simulation is indeed upper bounded by this maximum error demonstrating that the accuracy tracks the Chebyshev approximation error. The dashed line illustrates a supergeometric bound  $\mathcal{O}(e^{-d \log d})$ . This indicates that the accuracy  $\varepsilon$  is bounded by  $\mathcal{O}(e^{-d \log d})$ . Hence, we can choose degree  $d = \mathcal{O}(e^{W_0 \lceil \log(1/\varepsilon) \rceil}) = \mathcal{O}[\log(1/\varepsilon)]$  for a fixed target error  $0 < \varepsilon < 1$  with  $W_0$  the principal branch of the Lambert W function. As a rule-of-thumb we expect at least geometric convergence to hold for analytic functions.

Figure 7(c) shows the number of two-qubit gates for varying degrees and different grid sizes. Circuits are compiled with pytket for the default native gate set of the H2-1 quantum computer at optimization level 2 [59]. The default native two-qubit gate is  $ZZ\text{Phase}(\theta) = e^{-i\frac{\theta}{2}Z \otimes Z}$  with arbitrary angle  $\theta$ . We perform a least-square fit of the data to the scaling of two-qubit gates derived in Sec. 2.6,  $\alpha_0 + \alpha_1 D 2^{\lceil \log_2(d+1) \rceil} n \lceil \log_2 n \rceil + \alpha_2 2^{D \lceil \log_2(d+1) \rceil}$ , where  $\alpha_0, \alpha_1, \alpha_2$  are the fitted parameters and we added a constant offset. The fit in Fig. 7(c) shows good agreement. For large  $n$  and  $d$  this scaling law is upper bounded by the simplified expression in Table 1. The

best parameters from the fit (see caption of Fig. 7) are in line with expectations from a worst-case analysis. For example, the term  $\alpha_2 2^{D \lceil \log_2(d+1) \rceil}$  comes from the implementation of the operators  $A$ ,  $C$ ,  $A^\dagger$  in Fig. 5 and the value  $\alpha_2 = 3$  indicates that each of the operators is implemented with the expected worst-case cost  $2^{D \lceil \log_2(d+1) \rceil}$ . We note some residual variance in the coefficients  $\alpha_0$  and  $\alpha_1$  depending on  $n$ , which we attribute to suppressed, non-dominant terms and compiler optimizations. The total number of qubits can be computed from Table 1. For example, the largest circuit in Fig. 7(c) at  $d = 63$ ,  $n = 6$  requires 30 qubits (12 for the main register and 18 for ancilla registers). The success probability shown in Fig. 7(d) saturates at around 8%, which is close to the asymptotic success probability for  $n \rightarrow \infty$  and  $d \rightarrow \infty$ . We compute the asymptotic success probability as  $p_{\text{success}}^* = \int_{[-1,1]^2} dx dy |f(x,y)|^2 / 4 \left( \sum_{k,l=0}^{30} |c_{k,l}| \right)^2$ , which is the continuous version of Eq. (32). The sum in the numerator runs to  $k, l = 30$  because higher-order coefficients do not contribute noticeably and fall off super-exponentially. The factor  $1/4$  is from the size of the integration domain.

### 3.2 Bivariate Student's t-distribution via Fourier series

To illustrate the Fourier approach, we consider the bivariate non-standardized Student's t-distribution with one degree of freedom ( $\nu = 1$ , this is also known as the bivariate Cauchy distribution)

$$f(\mathbf{x}) = \frac{1}{2\pi\sqrt{\det(\Sigma)}} [1 + (\mathbf{x} - \boldsymbol{\mu})^T \Sigma^{-1} (\mathbf{x} - \boldsymbol{\mu})]^{-\frac{3}{2}}, \quad (35)$$

where  $\mathbf{x} = (x, y)^T$  and  $\boldsymbol{\mu}$  and  $\Sigma$  are location and scale parameters, respectively. Student's t-distribution is characterized by heavy tails with applications in finance to model heavy-tailed return distributions [60] among others.

For the Fourier approach we focus on the domain  $\mathbf{x} \in [0, 1]^2$  and choose  $\boldsymbol{\mu} = (0.5, 0.5)^T$  and,  $\Sigma = \begin{pmatrix} 0.05 & 0 \\ 0 & 0.05 \end{pmatrix}$ . Note that the bivariate Student's t-distribution does not factorize into two univariate Student's t-distributions. First, we periodically extend the function from  $[0, 1]^2$  to  $[-1, 1]^2$ , interpolate it with the Fourier series in Eq. (3) and compute coefficients with the fast Fourier transform following Appendix B. We choose the same degree and same grid size in each variable, i.e.  $d_x = d_y = d$  and  $n_x = n_y = n$ . Figure 8 shows the results of approximating the periodically extended Student's t-distribution by a Fourier series of varying degree  $d$  and for different grid sizes  $2^n \times 2^n$ . The maximum error in Fig. 8(b) scales asymptotically as  $\mathcal{O}(1/d)$ . This is caused by the periodic extension introducing a discontinuity in the first derivative of the extended function at the boundaries  $x = 0, 1$  and  $y = 0, 1$ . In the univariate case a rule-of-thumb is that for  $k-1$  times continuously differentiable functions and a  $k$ -th derivative with bounded variation, the asymptotic interpolation error is  $\mathcal{O}(1/d^k)$  [49, see Theorem 7.2 for an equivalent statement for Chebyshev interpolants]. Our numerics indicate this also holds for the bivariate case of the considered function. To reach higher convergence rate we could e.g. adjust the periodic extension method to smoothen the sharp corners at the boundaries.

Figure 8(c) shows the number of two-qubit gates after compilation to the Quantinuum native gate set with optimization level 2. A least-square fit of the data to the scaling of two-qubits gates derived in Sec. 2.6,  $\alpha_0 + \alpha_1 D n [\log_2(2d+1)] + \alpha_2 2^D [\log_2(2d+1)]$ , shows excellent agreement. The small coefficients  $\alpha_1 < 1$  (see caption of Fig. 8) indicate savings from the compilation step. As in the Chebyshev case,  $\alpha_2 \approx 3$  indicates worst-case synthesis of the operators  $A$ ,  $C$ ,  $A^\dagger$  in the LCU on the coefficient registers. The largest circuit in Fig. 8(c) at  $d = 63$ ,  $n = 6$  requires 26 qubits – 12 for the main register and 14 for the ancilla register, cf. Table 1.

Similar to the Chebyshev case the success probability in Fig. 8(d) saturates close to its asymptotic value of  $p_{\text{success}}^* = 7.52\%$ . This is computed as  $p_{\text{success}}^* = \int_{[0,1]^2} dx dy |f(x, y)|^2 / (\sum_{k,l=-63}^{63} |c_{k,l}|)^2$ . The sum runs to degree 63 because the coefficients beyond this degree did not contribute noticeably (tested up to  $k, l = 128$ ) and fall off with increasing degree.

### 3.3 Single electron in periodic 3D Coulomb potential

Our protocols are applicable even when the exact target function is unknown, but we have access to the coefficients of an approximation by other means, e.g. through the solution of a differential equation. To demonstrate this, in this section we use our Fourier approach for the preparation of wavefunctions of a single electron in a 3D translationally invariant Coulomb potential.

The prepared quantum state can serve as an initial state for the quantum simulation of materials in a unit cell of atoms with nuclear electronic Coulomb interactions. The unit cell wavefunction with cell volume equal to 1, is expressed as a linear combination of  $N^3$  plane wave basis functions via

$$\psi(\mathbf{r}) = \sum_{\mathbf{k} \in G} c_{\mathbf{k}} e^{i\pi \mathbf{k}^T \mathbf{r}}. \quad (36)$$

Here,  $\mathbf{k} = (k_x, k_y, k_z)^T$  runs over  $G = [-\frac{N}{2}, \frac{N-1}{2}]^3 \subset \mathbb{Z}^3$ ,  $\mathbf{r} = (x, y, z)^T \in [0, 1]^3$  is the real-space position of the electron in the unit cell. Equation (36) is a trigonometric polynomial in 3 variables with maximal degree  $N/2$  in each dimension, to which we apply our Fourier approach.

In order to obtain the coefficients  $c_{\mathbf{k}}$ , we insert the expansion (36) into the time-independent Schrödinger equation and solve the resulting set of linear equations. In the plane wave basis the kinetic energy matrix is diagonal with entries given by

$$T_{\mathbf{k}, \mathbf{k}} = \frac{(\hbar\pi\|\mathbf{k}\|)^2}{2m} |\mathbf{k}\rangle\langle\mathbf{k}|. \quad (37)$$

The electron-nuclear attraction matrix elements have the following convenient analytical form in the basis of plane waves

$$U_{\mathbf{k}, \mathbf{k}'} = \frac{4}{\pi} \sum_{\ell=1}^L w_{\ell} \frac{e^{i\pi(\mathbf{k}' - \mathbf{k})^T \mathbf{R}_{\ell}}}{\|\mathbf{k} - \mathbf{k}'\|^2} |\mathbf{k}\rangle\langle\mathbf{k}'|. \quad (38)$$

$\mathbf{R}_{\ell}$  is the position of nucleus  $\ell$  in real space and  $w_{\ell}$  is the corresponding nuclear weight and  $L$  is the number of nuclei. The  $\pi$  factors arise from the definition of the state in Eq. (36).

The electronic Hamiltonian matrix elements are then given by  $H_{\mathbf{k}, \mathbf{k}'}^{(\text{el})} = -T_{\mathbf{k}, \mathbf{k}} \delta_{\mathbf{k}, \mathbf{k}'} - U_{\mathbf{k}, \mathbf{k}'}$  and the time-independent Schrödinger equation becomes  $H^{(\text{el})} \mathbf{c} = E \mathbf{c}$  with  $\mathbf{c}$  the vector of coefficients in

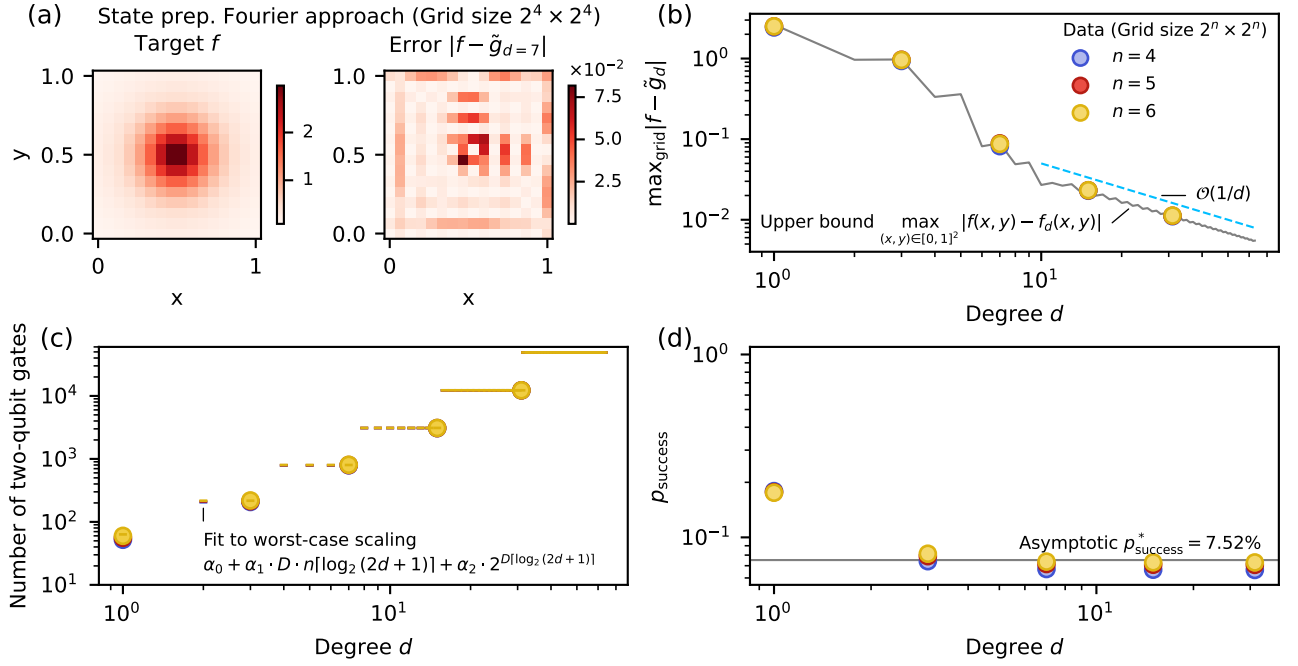


Figure 8: Resources for preparing an approximation to the bivariate Student's t-distribution with a 2D Fourier series approximation of degree  $d$  in each dimension. (a) Discretized target function and the difference to the rescaled amplitudes from a noiseless simulation of the algorithm for  $d = 7$ . (b) Maximum absolute error of the prepared state evaluated at the grid points for different grid sizes. The difference between the prepared state and the Fourier approximation is at machine precision (not shown). Hence, the maximum error of the noiseless simulation against the target function is upper bounded by the maximum error of the degree- $d$  Fourier interpolant over the (non-discretized) domain (grey line – floored at machine precision). The dashed line illustrates the asymptotic error bound  $\mathcal{O}(1/d)$ . (c) Two-qubit gate count of the algorithm for different grid sizes compiled with pytket optimization level 2 for the H2-1 gate set. The line markers are a least-square fit of the data (round markers) to the worst-case scaling with  $\alpha_0 = -4.91, -4.91, -4.91$ ,  $\alpha_1 = 0.78, 0.82, 0.85$ ,  $\alpha_2 = 2.99, 2.99, 2.99$  for  $n = 4, 5, 6$  and  $D = 2$ . (d) Empirical (markers) and asymptotic success probability for  $n \rightarrow \infty$  and  $d \rightarrow \infty$  (line).

Eq. (36). Solutions  $c$  for the first and second lowest eigenenergies result in the upper bounds to the ground and excited state wavefunction of the non-interacting single electronic system. We use those coefficients in our multivariate Fourier approach to prepare the quantum states for the ground and first excited state wavefunctions.

We choose the simplest 3D periodic unit cell for demonstration, which is a single Coulomb potential of nuclear weight and charge 1 at the center of a  $(1 \times 1 \times 1)$  unit cell at position  $(0.5, 0.5, 0.5)$ . Other more advanced unit cells can be used, such as face-centered cubic (FCC). In the left panels of Fig. 9 we present the real part of the ground (top) and first excited state wavefunctions (bottom) computed directly with Eq. (36) and coefficients from the solution of the time-independent Schrödinger equation above. We then use the same set of coefficients to construct the circuits of our Fourier-based protocol for preparing those wavefunctions. In the right panels of Fig. 9 we present the real part of the resulting wavefunctions obtained from a statevector simulation of those circuits. The simulated circuits replicate to numerical precision the results from the direct numerical computation.

Table 2 shows the resource requirements from compilation of the circuits of our method for preparing the wavefunctions with different numbers of grid points and coefficients. `pytket` [59] is used to construct the circuits, using the gateset  $\{CX, R_Z, R_X\}$ . This confirms that the dominant cost of the algorithm comes from the addition of the ancilla qubits that contain the Fourier coefficients, which is expected from Table 1. Increasing the spatial resolution (given by  $2^{3n}$ , where  $n$  is the number of qubits per spatial dimension), leads to little increase in gate count due to the efficient control structure presented in Fig 2. Using a total of 9 and 12 ancilla qubits (i.e. registers of size  $a = 3, 4$  per dimension) allows one to encode 512 and 4096 Fourier coefficients, respectively. Thus, the large increase in the number of gates is due to the 9 vs. 12 qubit circuits for  $A$ ,  $C$  and  $A^\dagger$  (cf. the term  $\mathcal{O}(d^D)$  for two-qubit gates in Table 1). For the 30 qubit case marked with \*, the success probability of generating the ground ( $\Psi_0$ ) and first excited ( $\Psi_1$ ) states are 0.7047 and 0.2392, respectively.

Although these are only single electron wavefunctions, they can be used as a starting point for many-electron wavefunctions by anti-symmetrizing the spatial registers of multiple single electron states follow-

| $n$ | $a$ | $D$ | Grid points ( $2^{Dn}$ ) | Coefficients ( $2^{Da}$ ) | Total qubits ( $Dn + Da$ ) | Two-qubit gates |
|-----|-----|-----|--------------------------|---------------------------|----------------------------|-----------------|
| 4   | 3   | 3   | 4096                     | 512                       | 21                         | 1602            |
| 5   | 3   | 3   | 32 768                   | 512                       | 24                         | 1620            |
| 6   | 3   | 3   | 262 144                  | 512                       | 27                         | 1638            |
| * 7 | 3   | 3   | 2 097 152                | 512                       | 30                         | 1656            |
| 7   | 4   | 3   | 2 097 152                | 4096                      | 33                         | 12 450          |

Table 2: Circuit compilation results for the solutions of the Schrödinger equation in a 3D periodic Coulomb potential with varying numbers of grid points and Fourier coefficients. With  $n$  the number of qubits per spatial dimension and  $a = \lceil \log_2 N \rceil$  the number of ancillas per dimension the total number of qubits is  $3n + 3a$ . The number of two-qubit gates is determined by compiling the circuits to the gate set given in the main text. The row marked with \* corresponds to the setting of Fig. 9.

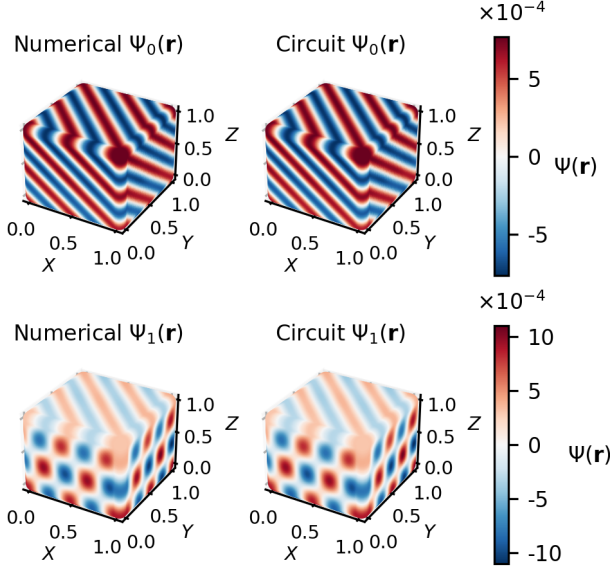


Figure 9: Real parts of the ground state (top panels) and first excited state (bottom) electronic wavefunctions for a unit cell with a single nucleus at the center at  $(0.5, 0.5, 0.5)$ . Left panels: direct evaluation of Eq. (36) with a total of  $N^3 = 512$  coefficients from the numerical solution of the time-independent Schrödinger equation. Right panels: equivalent solutions from the Fourier approach of our method evaluated with a statevector simulator using  $n = 7$  qubits per spatial dimension and  $a = 3$  ancilla qubits per dimension for a total of 30 qubits.

ing the procedure proposed in Ref. [61], or as the initial state for real or imaginary time evolution under an interacting electron Hamiltonian in the first quantized picture.

### 3.4 Bivariate Gaussian on quantum hardware

This section demonstrates our state preparation protocol on the H2-1 trapped-ion quantum computer and illustrates the effect of noise. We focus on analyzing the output signal without any error mitigation. Error mitigation protocols, if needed, would likely be performed in combination with a downstream quantum algorithm, not after state preparation, which is only the first step of the computation.

We choose a two-dimensional Gaussian distribution

as a target function. The low overheads of our method allow us to prepare the Gaussian on a fine grid with 24 qubits using up to 237 two-qubit gates with meaningful output signal. The Gaussian distribution is given by

$$f(\mathbf{x}) = \frac{1}{2\pi\sqrt{\det(\Sigma)}} \exp\left[-\frac{1}{2}(\mathbf{x} - \boldsymbol{\mu})^T \Sigma^{-1}(\mathbf{x} - \boldsymbol{\mu})\right], \quad (39)$$

where  $\mathbf{x} = (x, y)^T$ ,  $\boldsymbol{\mu}$  is the mean and  $\Sigma$  is the positive semi-definite covariance matrix. Let  $Z = X \times Y$  be a 2D random variable distributed according to  $f(x, y)$ . The covariance matrix can be parametrized by the marginal variances  $\sigma_x^2 = \text{Var}(X)$  and  $\sigma_y^2 = \text{Var}(Y)$  (diagonal entries of  $\Sigma$ ), and the (Pearson) correlation coefficient  $\rho = \text{Cov}(X, Y)/\sigma_x\sigma_y$  (setting off-diagonal entries  $\rho\sigma_x\sigma_y$ ). For this demonstration, we use  $\boldsymbol{\mu} = (\mu_x, \mu_y)^T = (0.5, 0.5)^T$ ,  $\sigma_x = 0.22$ ,  $\sigma_y = 0.18$ , and the two choices  $\rho = 0.0$  and  $\rho = 0.4$ . The first setting defines an uncorrelated Gaussian, i.e. the bivariate density  $f(x, y)$  is the product of two univariate densities. The second setting defines a correlated Gaussian, which does not factorize.

For both settings we use  $n_x = n_y = 9$  qubits for spatial discretization of the domain  $[0, 1]^2$  (cf. Fig. 5) into  $512 \times 512 = 262 144$  grid points (for comparison, Ref. [44] prepared a bivariate function on a grid of size  $32 \times 32$ ). We use a Fourier series approximation  $f_d(x, y)$  of degrees  $d = d_x = d_y = 3$ , which leads to a total of  $(2d+1)^2 = 49$  coefficients. Note that we use a different method to compute the Fourier coefficients than the one used in Sec. 3.2 because the approximation at the chosen degree is better for the specific target, see Appendix C.2. To encode the Fourier coefficients we require ancilla registers with  $a_x = a_y = 3$  qubits each, cf. Fig. 5. Overall, this results in a circuit with 24 qubits. We test our approach on the H2-1 trapped-ion quantum computer [62, 63]. At the time of this demonstration in April and May 2024, it provides 32 fully-connected qubits with average single- and two-qubit gate infidelities of  $3 \times 10^{-5}$  and  $2 \times 10^{-3}$ , respectively, and average state preparation and measurement error of  $2 \times 10^{-3}$ . Detailed specifications are given in Appendix C.1.

The Fourier approximation  $f_{d=3}(x, y)$  of the (positive) Gaussian density in Eq. (39) can have noticeable

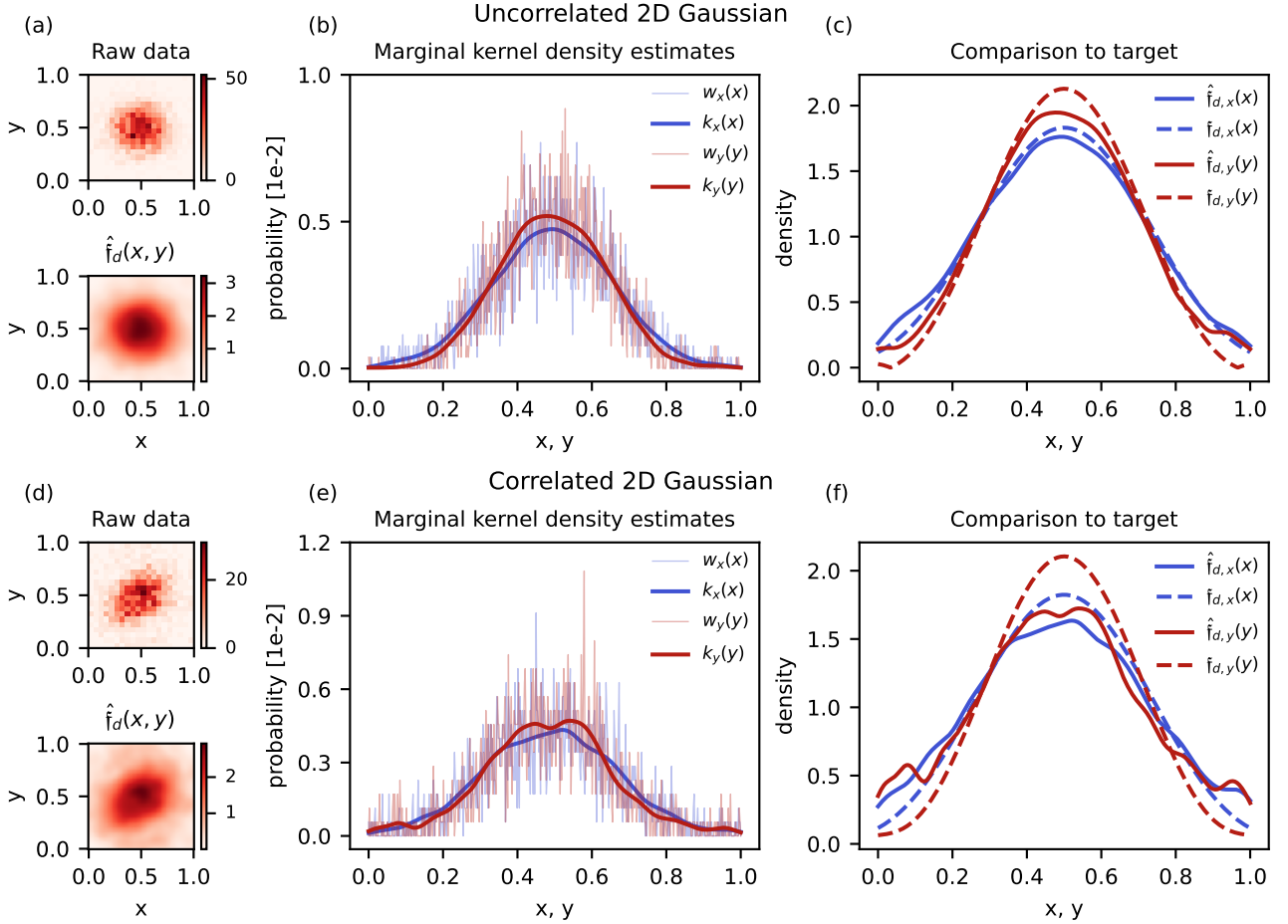


Figure 10: Experimental results for preparing a 2D Fourier series approximation of the bivariate Gaussian distribution. We show two setting, an uncorrelated Gaussian (upper panel) and a correlated Gaussian (lower panel); parameters are given in the main text. (a, d) Histograms of the raw two-dimensional measurement counts with 50 bins along each axis (upper plots), and the resulting estimates  $\hat{f}_d(x, y)$  (lower plots, obtained from kernel density estimates) of the target functions  $f_d(x, y)$ . (b, e) Marginal probabilities  $w_x(x), w_y(y)$  of the measurement data (thin solid lines) and the corresponding kernel density estimates  $k_x(x), k_y(y)$  (bold solid lines). (c, f) Direct comparison between marginal estimates  $\hat{f}_{d,x}(x), \hat{f}_{d,y}(y)$  (solid lines) and the target functions' marginals  $f_{d,x}(x), f_{d,y}(y)$  (dashed lines).

negative values in  $[0, 1]^2$ . This is visible in the small kinks of the red dashed line (showing a marginal over  $|f_d(x, y)|$ ) in Fig. 10(c) close to the boundaries of the domain  $[0, 1]$ . To avoid expensive state-tomographic methods, we only read out the magnitudes  $|f_d(x, y)|$  of the Fourier series via measurements in the computational basis and compare our experimental data to the positive target function  $f_d(x, y) = |f_d(x, y)|$ . We run each experiment with 20 000 shots. The success probability in our setting is around 10% (for details see Appendix C.2). Let  $w(x_i, y_j)$  be the probability to measure grid point  $(x_i, y_j) \in [0, 1]^2, i, j = 1, \dots, 512$ , after post-selection on the zero state in the ancilla register (cf. Fig. 4), and let  $w_x(x_i) = \sum_{j=1}^{512} w(x_i, y_j)$ ,  $w_y(y_j) = \sum_{i=1}^{512} w(x_i, y_j)$  be its marginals. The upper panels of Fig. 10(a) and (d) show histograms of the joint measurement distribution  $w(x, y)$  for the uncorrelated and correlated settings, respectively. Figures 10(b) and (e) show the corresponding  $x$ - and  $y$ -marginals as thin lines. Notably, the measured signals

suffer from substantial fluctuations due to shot noise.

To compare the empirical probabilities to the target  $f_d(x, y)$  in a meaningful way, we smoothen the experimental data with kernel density estimation (KDE) [64–66]. The KDE yields a continuous approximation of the density underlying a finite data sample. This is obtained by replacing the raw counts with, in our case, Gaussian kernels of a given bandwidth  $h$  (see Appendix C.3). The KDE becomes smoother with increasing bandwidth  $h$ . On the other hand, for too large  $h$  the KDE loses information about the underlying data. In the limit  $h \rightarrow \infty$ , the KDE approaches a perfectly flat distribution. The “optimal” bandwidth can be computed via minimization of an appropriate cost function. A naive choice would be, for example, to consider a distance measure or statistical divergence (such as the relative entropy) between KDE and the target function  $f_d(x, y)$ . However, this choice introduces an obvious bias. Instead we choose to optimize  $h$  via cross validation from the measurement



|                     |                   | $\mu_{d,x}, \hat{\mu}_{d,x}$ | $\mu_{d,y}, \hat{\mu}_{d,y}$ | $\sigma_{d,x}^2, \hat{\sigma}_{d,x}^2$ | $\sigma_{d,y}^2, \hat{\sigma}_{d,y}^2$ | $\rho_d, \hat{\rho}_d$ | $F_x$ | $F_y$ | $F$   |
|---------------------|-------------------|------------------------------|------------------------------|--|--|------------------------|-------|-------|-------|
| <b>Uncorrelated</b> | $f_d(x, y)$       | 0.5                          | 0.5                          | 0.0413                                 | 0.0299                                 | 0.0                    | 0.998 | 0.984 | 0.986 |
| <b>Gaussian</b>     | $\hat{f}_d(x, y)$ | 0.494                        | 0.495                        | 0.0468                                 | 0.0396                                 | -0.015                 |       |       |       |
| <b>Correlated</b>   | $f_d(x, y)$       | 0.5                          | 0.5                          | 0.0415                                 | 0.0321                                 | 0.353                  | 0.991 | 0.963 | 0.918 |
| <b>Gaussian</b>     | $\hat{f}_d(x, y)$ | 0.493                        | 0.488                        | 0.0519                                 | 0.0510                                 | 0.088                  |       |       |       |

Table 3: Experimental results for preparing a 2D Fourier series approximation of the bivariate Gaussian distribution, see Fig. 10. We consider two settings, the preparation of an uncorrelated and a correlated Gaussian. The table collects, for both settings, mean values, variances and correlation coefficients [cf. Eq. (40)] of the target densities  $f_d(x, y)$  and their estimates  $\hat{f}_d(x, y)$ , based on kernel density estimation. Moreover, we show the fidelities  $F_x, F_y$  [cf. Eq. (41)] between marginal estimates,  $\hat{f}_{d,x}, \hat{f}_{d,y}$ , and target functions' marginals,  $f_{d,x}, f_{d,y}$ , and the full fidelity  $F$  between  $\hat{f}_d$  and  $f_d$  [cf. Eq. (41)].

data alone (see Appendix C).

Let  $k(x, y)$ ,  $k_x(x)$  and  $k_y(y)$  be the KDE [cf. Eq. (57)] corresponding to the empirical probabilities  $w(x_i, y_j)$ ,  $w_x(x_i)$  and  $w_y(y_j)$  ( $i, j = 1, \dots, 512$ ), rescaled such that  $\sum_{i,j=1}^{512} k(x_i, y_j) = \sum_{i=1}^{512} k_x(x_i) = \sum_{j=1}^{512} k_y(y_j) = 1$ . The thick solid lines in Figs. 10(b) and (e) are the marginal KDE  $k_x(x_i)$  and  $k_y(y_j)$ . To compare to  $f_d(x, y)$ , we need to take the square root, which defines our experimental estimates  $\hat{f}_d(x, y) = \sqrt{k(x, y)}$ ,  $\hat{f}_{d,x}(x) = \sqrt{k_x(x)}$  and  $\hat{f}_{d,y}(y) = \sqrt{k_y(y)}$ . The lower panels of Fig. 10(a) and (d) display  $\hat{f}_d(x, y)$ . In Fig. 10(c) and (f), we compare the estimated marginals (solid lines) to the target marginals  $f_{d,x}, f_{d,y}$  of  $f_d$  (dashed lines). For direct comparison, we rescale all functions  $\hat{f}_d, \hat{f}_{d,x}, \hat{f}_{d,y}, f_{d,x}, f_{d,y}$  such that they integrate to one on their corresponding domains, i.e. that they represent proper probability densities. Visually, we observe a good agreement. We clearly recognize an elongated shape in the lower plot of Fig. 10(d), as expected from a correlated 2D Gaussian.

For a quantitative comparison we determine the mean values and the covariance matrix of the target function  $f_d(x, y)$  and its estimate  $\hat{f}_d(x, y)$  (obtained from the experimental data):

$$\begin{aligned}
\mu_{d,x} &= \int_{[0,1]^2} dx dy x f_d(x, y), \\
\mu_{d,y} &= \int_{[0,1]^2} dx dy y f_d(x, y), \\
\sigma_{d,x}^2 &= \int_{[0,1]^2} dx dy (x - \mu_{d,x})^2 f_d(x, y), \\
\sigma_{d,y}^2 &= \int_{[0,1]^2} dx dy (y - \mu_{d,y})^2 f_d(x, y), \\
\rho_d &= \frac{\int_{[0,1]^2} dx dy (x - \mu_{d,x})(y - \mu_{d,y}) f_d(x, y)}{\sigma_{d,x} \sigma_{d,y}},
\end{aligned} \tag{40}$$

and  $\hat{\mu}_{d,x}, \hat{\mu}_{d,y}, \hat{\sigma}_{d,x}^2, \hat{\sigma}_{d,y}^2, \hat{\rho}_d$  computed equivalently by replacing all quantities with their “hat” versions (e.g. replace  $f_d(x, y)$  with  $\hat{f}_d(x, y)$ ). Furthermore, we compute the classical fidelity between the target and mea-

surements

$$F = \frac{\left( \sum_{i,j=1}^{512} \sqrt{f_d(x_i, y_j) \hat{f}_d(x_i, y_j)} \right)^2}{\sum_{i,j=1}^{512} f_d(x_i, y_j) \sum_{i,j=1}^{512} \hat{f}_d(x_i, y_j)}, \tag{41}$$

where  $x_i, y_i$  runs over the grid points. Table 3 compares the results for both settings. Overall, we observe a good agreement between the targets and the experimentally prepared functions, both in terms of statistical quantifiers and fidelities. For the uncorrelated 2D Gaussian we obtain an overall fidelity of  $F = 0.986$ , for the correlated one we obtain  $F = 0.918$ .

We observe a larger deviation between target and prepared function for the correlated Gaussian. For example, the observed variances  $\hat{\sigma}_{d,x}^2, \hat{\sigma}_{d,y}^2$  overestimate the target variances  $\sigma_{d,x}^2, \sigma_{d,y}^2$  in this setting. Although we clearly identify a non-zero correlation coefficient in the setting of the correlated Gaussian, the estimated  $\hat{\rho}_d = 0.088$  is significantly smaller, roughly by a factor of four, than the target value  $\rho_d = 0.353$ . The pronounced discrepancy between  $f_d$  and  $\hat{f}_d$  in the correlated setting, in comparison to the uncorrelated Gaussian, is expected. This is because, in the latter scenario, we are able to exploit the factorization of  $f_d(x, y)$  into two univariate functions also at the level of circuit synthesis. Indeed we obtain much shallower circuits for the uncorrelated setting, which are much less prone to noise, as discussed in more detail in App. C.2.

## 4 Conclusions

This work introduces methods for the preparation of quantum states that encode multivariate functions, and analyzes their resource requirements. As a proof-of-concept, we demonstrate the successful preparation of representative initial states (with potential applications e.g. in quantum chemistry, physics and finance simulations) on comparatively high-resolution grids. We execute a 24-qubit experiment on Quantinuum’s H2-1 trapped-ion quantum computer and analyse the impact of noise on the prepared states.

Many functions of interest cannot be naturally encoded in a quantum state (e.g.  $1/x$  due to a singularity), and function approximation becomes a necessary step to obtain practical protocols. Our methods are based on multivariate versions of Fourier and Chebyshev series approximations. We note that power series can be mapped to Chebyshev series [67, 68] where our method applies as-is. Walsh series used e.g. in [46, 47] can be implemented as a special case of our Fourier method. It is also possible to use different basis functions for each dimension in a hybrid Fourier-Chebyshev method. Moreover, the building blocks of our method can be applied recursively to create more expressive basis functions, e.g. wavelets and kernels, which are then linearly combined to form more complex functions. Ultimately, the approximation method and error budget will depend on the use case (e.g. whether the target function is periodic) and specifics of the available quantum hardware (e.g. two-qubit gate fidelity).

QSP [35–39] has attracted significant interest as a framework for developing quantum algorithms via polynomial transformations of block-encoded matrices. Multivariate versions of QSP have been proposed and analyzed, although questions about expressive power remain open [41–43]. Our work shows that linear combination of unitaries [50], with its simplicity and effectiveness, is a valid alternative for the task of preparing quantum states that encode multivariate functions in their amplitudes. An interesting research direction consists of using (univariate) QSP to further process the matrices produced by our method. For example, suppose we wanted to prepare a state that encodes a hypersurface – a set of dimension  $(D - 1)$  defined by a polynomial equation of the form  $f(x_1, \dots, x_D) = 0$ . After discretizing each dimension via  $H^{\otimes D}$  and using our method to construct the diagonal operator  $f(H^{\otimes D})$ , we use QSP to filter its eigenvalues. In particular, we want a polynomial  $p$  such that  $p(0) = 1$  and  $|p(y)|$  is small for  $y \in [-1, -\epsilon] \cup [\epsilon, 1]$ . An optimal filter is given by Lin and Tong in [69]. Applying the resulting operator to the uniform superposition we obtain a state proportional to  $\sum_{x_1} \dots \sum_{x_D} p(f(x_1, \dots, x_D)) |x_1, \dots, x_D\rangle$ , approximately encoding the hypersurface. Remarkably, this proposal uses univariate QSP for a fundamentally multivariate problem.

## Acknowledgements

We thank Alexandre Krajenbrink and Enrico Rinaldi for helpful feedback on the manuscript.

## References

- [1] Sarah K. Leyton and Tobias J. Osborne. “A quantum algorithm to solve nonlinear differential equations” (2008). [arXiv:0812.4423](#).
- [2] Andrew M. Childs, Jin-Peng Liu, and Aaron Ostrander. “High-precision quantum algorithms for partial differential equations”. *Quantum* **5**, 574 (2021).
- [3] Dylan Herman, Cody Googin, Xiaoyuan Liu, Alexey Galda, Ilya Safro, Yue Sun, Marco Pistoia, and Yuri Alexeev. “A survey of quantum computing for finance” (2022). [arXiv:2201.02773](#).
- [4] Nikitas Stamatopoulos and William J. Zeng. “Derivative Pricing using Quantum Signal Processing”. *Quantum* **8**, 1322 (2024).
- [5] Ismail Yunus Akhalwaya, Adam Connolly, Roland Guichard, Steven Herbert, Cahit Kargi, Alexandre Krajenbrink, Michael Lubasch, Conor Mc Keever, Julien Sorci, Michael Spranger, and Ifan Williams. “A Modular Engine for Quantum Monte Carlo Integration” (2023). [arXiv:2308.06081](#).
- [6] Alán Aspuru-Guzik, Anthony D. Dutoi, Peter J. Love, and Martin Head-Gordon. “Simulated quantum computation of molecular energies”. *Science* **309**, 1704–1707 (2005).
- [7] Ivan Kassal, Stephen P. Jordan, Peter J. Love, Masoud Mohseni, and Alán Aspuru-Guzik. “Polynomial-time quantum algorithm for the simulation of chemical dynamics”. *Proceedings of the National Academy of Sciences* **105**, 18681–18686 (2008).
- [8] Yudong Cao, Jonathan Romero, Jonathan P Olson, Matthias Degroote, Peter D Johnson, Mária Kieferová, Ian D Kivlichan, Tim Menke, Borja Peropadre, Nicolas P D Sawaya, Sukin Sim, Libor Veis, and Alán Aspuru-Guzik. “Quantum chemistry in the age of quantum computing”. *Chem. Rev.* **119**, 10856–10915 (2019).
- [9] Sam McArdle, Suguru Endo, Alán Aspuru-Guzik, Simon C Benjamin, and Xiao Yuan. “Quantum computational chemistry”. *Rev. Mod. Phys.* **92**, 015003 (2020).
- [10] Jie Liu, Yi Fan, Zhenyu Li, and Jinlong Yang. “Quantum algorithms for electronic structures: basis sets and boundary conditions”. *Chem. Soc. Rev.* **51**, 3263–3279 (2022).
- [11] Stephen P. Jordan, Keith S. M. Lee, and John Preskill. “Quantum algorithms for quantum field theories”. *Science* **336**, 1130–1133 (2012).
- [12] Mari Carmen Bañuls, Rainer Blatt, Jacopo Catani, Alessio Celi, Juan Ignacio Cirac, Marcello Dalmonte, Leonardo Fallani, Karl Jansen, Maciej Lewenstein, Simone Montangero, Christine A. Muschik, Benni Reznik, Enrique Rico, Luca Tagliacozzo, Karel Van Acoleyen, Frank Verstraete, Uwe-Jens Wiese, Matthew Wingate, Jakub Zakrzewski, and Peter Zoller. “Simulating lattice gauge theories within quantum technologies”. *The European Physical Journal D* **74**, 165 (2020).

- [13] Christian W. Bauer, Zohreh Davoudi, A. Baha Balantekin, Tanmoy Bhattacharya, Marcela Carena, Wibe A. de Jong, Patrick Draper, Aida El-Khadra, Nate Gemelke, Masanori Hanada, Dmitri Kharzeev, Henry Lamm, Ying-Ying Li, Junyu Liu, Mikhail Lukin, Yannick Meurice, Christopher Monroe, Benjamin Nachman, Guido Pagano, John Preskill, Enrico Rinaldi, Alessandro Roggero, David I. Santiago, Martin J. Savage, Irfan Siddiqi, George Siopsis, David Van Zanten, Nathan Wiebe, Yukari Yamauchi, Kübra Yeter-Aydeniz, and Silvia Zorzetti. “Quantum simulation for high-energy physics”. *PRX Quantum* **4**, 027001 (2023).
- [14] Alexander M. Dalzell, Sam McArdle, Mario Berta, Przemyslaw Bienias, Chi-Fang Chen, András Gilyén, Connor T. Hann, Michael J. Kastoryano, Emil T. Khabiboulline, Aleksander Kubica, Grant Salton, Samson Wang, and Fernando G. S. L. Brandão. “Quantum algorithms: A survey of applications and end-to-end complexities” (2023). [arXiv:2310.03011](#).
- [15] Juha J. Vartiainen, Mikko Möttönen, and Martti M. Salomaa. “Efficient decomposition of quantum gates”. *Phys. Rev. Lett.* **92**, 177902 (2004).
- [16] Mikko Möttönen, Juha J. Vartiainen, Ville Bergholm, and Martti M. Salomaa. “Transformation of quantum states using uniformly controlled rotations”. *Quant. Inf. Comp.* **5**, 467 (2005). [arXiv:quant-ph/0407010](#).
- [17] Ville Bergholm, Juha J. Vartiainen, Mikko Möttönen, and Martti M. Salomaa. “Quantum circuits with uniformly controlled one-qubit gates”. *Phys. Rev. A* **71**, 052330 (2005).
- [18] Vivek V. Shende, Stephen S. Bullock, and Igor L. Markov. “Synthesis of quantum-logic circuits”. *IEEE Transactions on Computer-Aided Design of Integrated Circuits and Systems* **25**, 1000–1010 (2006). [arXiv:quant-ph/0406176](#).
- [19] Martin Plesch and Časlav Brukner. “Quantum-state preparation with universal gate decompositions”. *Phys. Rev. A* **83**, 032302 (2011).
- [20] Guang Hao Low, Vadym Kliuchnikov, and Luke Schaeffer. “Trading T-gates for dirty qubits in state preparation and unitary synthesis” (2018). [arXiv:1812.00954](#).
- [21] Xiaoming Sun, Guojing Tian, Shuai Yang, Pei Yuan, and Shengyu Zhang. “Asymptotically optimal circuit depth for quantum state preparation and general unitary synthesis”. *IEEE Transactions on Computer-Aided Design of Integrated Circuits and Systems* **42**, 3301–3314 (2023).
- [22] Xiao-Ming Zhang, Tongyang Li, and Xiao Yuan. “Quantum state preparation with optimal circuit depth: Implementations and applications”. *Phys. Rev. Lett.* **129**, 230504 (2022).
- [23] Lov Grover and Terry Rudolph. “Creating superpositions that correspond to efficiently integrable probability distributions” (2002). [arXiv:quant-ph/0208112](#).
- [24] Alexei Kitaev and William A. Webb. “Wavefunction preparation and resampling using a quantum computer” (2009). [arXiv:0801.0342](#).
- [25] Arthur G. Rattew, Yue Sun, Pierre Minssen, and Marco Pistoia. “The Efficient Preparation of Normal Distributions in Quantum Registers”. *Quantum* **5**, 609 (2021).
- [26] Gabriel Marin-Sanchez, Javier Gonzalez-Conde, and Mikel Sanz. “Quantum algorithms for approximate function loading”. *Phys. Rev. Res.* **5**, 033114 (2023).
- [27] Adam Holmes and A. Y. Matsuura. “Efficient quantum circuits for accurate state preparation of smooth, differentiable functions” (2020). [arXiv:2005.04351](#).
- [28] Javier Gonzalez-Conde, Thomas W. Watts, Pablo Rodriguez-Grasa, and Mikel Sanz. “Efficient quantum amplitude encoding of polynomial functions”. *Quantum* **8**, 1297 (2024).
- [29] Jason Iaconis, Sonika Johri, and Elton Yechao Zhu. “Quantum state preparation of normal distributions using matrix product states”. *npj Quantum Information* **10**, 15 (2024).
- [30] Arthur G. Rattew and Bálint Koczor. “Preparing arbitrary continuous functions in quantum registers with logarithmic complexity” (2022). [arXiv:2205.00519](#).
- [31] Yuval R. Sanders, Guang Hao Low, Artur Scherer, and Dominic W. Berry. “Black-box quantum state preparation without arithmetic”. *Phys. Rev. Lett.* **122**, 020502 (2019).
- [32] Johannes Bausch. “Fast Black-Box Quantum State Preparation”. *Quantum* **6**, 773 (2022).
- [33] Jessica Lemieux, Matteo Lostaglio, Sam Pallister, William Pol, Karthik Seetharam, Sukin Sim, and Burak Şahinoğlu. “Quantum sampling algorithms for quantum state preparation and matrix block-encoding” (2024). [arXiv:2405.11436](#).
- [34] Shengbin Wang, Zhimin Wang, Guolong Cui, Shangshang Shi, Ruimin Shang, Lixin Fan, Wendong Li, Zhiqiang Wei, and Yongjian Gu. “Fast black-box quantum state preparation based on linear combination of unitaries”. *Quantum Information Processing* **20**, 270 (2021).
- [35] Guang Hao Low and Isaac L. Chuang. “Optimal Hamiltonian Simulation by Quantum Signal Processing”. *Phys. Rev. Lett.* **118**, 010501 (2017).
- [36] András Gilyén, Yuan Su, Guang Hao Low, and Nathan Wiebe. “Quantum singular value transformation and beyond: exponential improvements for quantum matrix arithmetics”. In Proceedings of the 51st Annual ACM SIGACT Symposium on Theory of Computing. ACM (2019). [arXiv:1806.01838](#).

- [37] Thais L. Silva, Márcio M. Taddei, Stefano Carrazza, and Leandro Aolita. “Fragmented imaginary-time evolution for early-stage quantum signal processors”. *Scientific Reports* **13**, 18258 (2023).
- [38] John M. Martyn, Zane M. Rossi, Andrew K. Tan, and Isaac L. Chuang. “Grand unification of quantum algorithms”. *PRX Quantum* **2**, 040203 (2021).
- [39] Yuta Kikuchi, Conor Mc Keever, Luuk Coopmans, Michael Lubasch, and Marcello Benedetti. “Realization of quantum signal processing on a noisy quantum computer”. *npj Quantum Information* **9** (2023).
- [40] Sam McArdle, András Gilyén, and Mario Berta. “Quantum state preparation without coherent arithmetic” (2022). [arXiv:2210.14892](#).
- [41] Zane M. Rossi and Isaac L. Chuang. “Multivariable quantum signal processing (M-QSP): prophecies of the two-headed oracle”. *Quantum* **6**, 811 (2022). [arXiv:2205.06261](#).
- [42] Hitomi Mori, Keisuke Fujii, and Kaoru Mizuta. “Comment on “Multivariable quantum signal processing (M-QSP): prophecies of the two-headed oracle”” (2023). [arXiv:2310.00918](#).
- [43] Balázs Németh, Blanka Kövér, Boglárka Kulcsár, Roland Botond Miklósi, and András Gilyén. “On variants of multivariate quantum signal processing and their characterizations” (2023). [arXiv:2312.09072](#).
- [44] Mudassir Moosa, Thomas W Watts, Yiyu Chen, Abhijat Sarma, and Peter L McMahon. “Linear-depth quantum circuits for loading fourier approximations of arbitrary functions”. *Quantum Science and Technology* **9**, 015002 (2023).
- [45] Juan José García-Ripoll. “Quantum-inspired algorithms for multivariate analysis: From interpolation to partial differential equations”. *Quantum* **5**, 431 (2021).
- [46] Julien Zylberman and Fabrice Debbausch. “Efficient Quantum State Preparation with Walsh Series” (2023). [arXiv:2307.08384](#).
- [47] Jonathan Welch, Daniel Greenbaum, Sarah Mostame, and Alan Aspuru-Guzik. “Efficient quantum circuits for diagonal unitaries without ancillas”. *New Journal of Physics* **16**, 033040 (2014).
- [48] John P. Boyd. “Chebyshev and Fourier Spectral Methods”. Dover Publications. Mineola, N.Y. (2001). 2nd revised edition.
- [49] Lloyd N. Trefethen. “Approximation Theory and Approximation Practice, Extended Edition”. *Other Titles in Applied Mathematics*. Society for Industrial and Applied Mathematics. Philadelphia, PA (2019).
- [50] Andrew M. Childs and Nathan Wiebe. “Hamiltonian simulation using linear combinations of unitary operations”. *Quantum Info. Comput.* **12**, 901–924 (2012). [arXiv:1202.5822](#).
- [51] Guang Hao Low and Isaac L. Chuang. “Hamiltonian simulation by qubitization”. *Quantum* **3**, 163 (2019).
- [52] Andrew M. Childs, Robin Kothari, and Rolando D. Somma. “Quantum algorithm for systems of linear equations with exponentially improved dependence on precision”. *SIAM Journal on Computing* **46**, 1920–1950 (2017).
- [53] William Kirby, Mario Motta, and Antonio Mezzacapo. “Exact and efficient Lanczos method on a quantum computer”. *Quantum* **7**, 1018 (2023).
- [54] Daan Camps, Lin Lin, Roel Van Beeumen, and Chao Yang. “Explicit quantum circuits for block encodings of certain sparse matrices”. *SIAM Journal on Matrix Analysis and Applications* **45**, 801–827 (2024). [arXiv:2203.10236](#).
- [55] Xiaoming Sun Junhong Nie, Wei Zi. “Quantum circuit for multi-qubit toffoli gate with optimal resource” (2024). [arXiv:2402.05053](#).
- [56] Yanghua Wang. “Generalized seismic wavelets”. *Geophysical Journal International* **203**, 1172–1178 (2015).
- [57] J. P. Antoine. “Wavelet analysis of signals and images, a grand tour”. *Ciencias Matemáticas* **18**, 113–144 (2000).
- [58] Lewis Wright, Conor Mc Keever, Jeremy T. First, Rory Johnston, Jeremy Tillay, Skylar Chaney, Matthias Rosenkranz, and Michael Lubasch. “Noisy intermediate-scale quantum simulation of the one-dimensional wave equation” (2024). [arxiv:2402.19247](#).
- [59] Seyon Sivarajah, Silas Dilkes, Alexander Cowtan, Will Simmons, Alec Edgington, and Ross Duncan. “T|ket>: A retargetable compiler for NISQ devices”. *Quantum Science and Technology* **6**, 014003 (2020). [arxiv:2003.10611](#).
- [60] Ching-Wai (Jeremy) Chiu, Haroon Mumtaz, and Gábor Pintér. “Forecasting with VAR models: Fat tails and stochastic volatility”. *International Journal of Forecasting* **33**, 1124–1143 (2017).
- [61] Hans Hon Sang Chan, Richard Meister, Tyson Jones, David P. Tew, and Simon C. Benjamin. “Grid-based methods for chemistry simulations on a quantum computer”. *Science Advances* **9**, eabo7484 (2023).
- [62] S. A. Moses, C. H. Baldwin, M. S. Allman, R. Ancona, L. Ascarrunz, C. Barnes, J. Bartolotta, B. Bjork, P. Blanchard, M. Bohn, J. G. Bohnet, N. C. Brown, N. Q. Burdick, W. C. Burton, S. L. Campbell, J. P. Campora, C. Caron, J. Chambers, J. W. Chan, Y. H. Chen, A. Chernoguzov, E. Chertkov, J. Colina, J. P. Curtis, R. Daniel, M. DeCross, D. Deen, C. Delaney, J. M. Dreiling, C. T. Ertsgaard, J. Esposito, B. Estey, M. Fabrikant, C. Figgatt, C. Foltz, M. Foss-Feig, D. Francois, J. P. Gaebler, T. M.



- Gatterman, C. N. Gilbreth, J. Giles, E. Glynn, A. Hall, A. M. Hankin, A. Hansen, D. Hayes, B. Higashi, I. M. Hoffman, B. Horning, J. J. Hout, R. Jacobs, J. Johansen, L. Jones, J. Karcz, T. Klein, P. Lauria, P. Lee, D. Liefer, S. T. Lu, D. Lucchetti, C. Lytle, A. Malm, M. Matheny, B. Mathewson, K. Mayer, D. B. Miller, M. Mills, B. Neyenhuis, L. Nugent, S. Olson, J. Parks, G. N. Price, Z. Price, M. Pugh, A. Ransford, A. P. Reed, C. Roman, M. Rowe, C. Ryan-Anderson, S. Sanders, J. Sedlacek, P. Shevchuk, P. Siegfried, T. Skripka, B. Spaun, R. T. Sprenkle, R. P. Stutz, M. Swallows, R. I. Tobey, A. Tran, T. Tran, E. Vogt, C. Volin, J. Walker, A. M. Zolot, and J. M. Pino. “A race-track trapped-ion quantum processor”. *Phys. Rev. X* **13**, 041052 (2023).
- [63] “Quantinuum System Model H2 Powered by Honeywell”. url: <https://www.quantinuum.com/hardware/h2>. (accessed: 2024-03-25).
- [64] Duin. “On the Choice of Smoothing Parameters for Parzen Estimators of Probability Density Functions”. *IEEE Transactions on Computers* **C-25**, 1175–1179 (1976).
- [65] Mats Rudemo. “Empirical choice of histograms and kernel density estimators”. *Scandinavian Journal of Statistics* **9**, 65–78 (1982). url: <http://www.jstor.org/stable/4615859>.
- [66] Trevor Hastie, Robert Tibshirani, and Jerome Friedman. “The Elements of Statistical Learning”. *Springer Series in Statistics*. Springer New York. New York, NY (2009).
- [67] Henry C. Thacher. “Conversion of a power to a series of Chebyshev polynomials”. *Commun. ACM* **7**, 181–182 (1964).
- [68] Hippolyte Nyengeri, Rénovat Nizigiyimana, Jean-Pierre Mutankana, Henry Bayaga, and Ferdinand Bayubahe. “Power and Chebyshev Series Transformation Formulas with Applications to Solving Ordinary Differential Equations via the Fröbenius and Taylor’s Methods”. *Open Access Library Journal* **8**, 1–19 (2021).
- [69] Lin Lin and Yu Tong. “Optimal polynomial based quantum eigenstate filtering with application to solving quantum linear systems”. *Quantum* **4**, 361 (2020).
- [70] D. Elliott, D.F. Paget, G.M. Phillips, and P.J. Taylor. “Error of truncated chebyshev series and other near minimax polynomial approximations”. *Journal of Approximation Theory* **50**, 49–57 (1987).
- [71] Alex Townsend and Lloyd N. Trefethen. “An Extension of Chebfun to Two Dimensions”. *SIAM Journal on Scientific Computing* **35**, C495–C518 (2013).
- [72] Lloyd N. Trefethen. “Multivariate polynomial approximation in the hypercube”. *Proceedings of the American Mathematical Society* **145**, 4837–4844 (2017).
- [73] Charles Fefferman. “On the convergence of multiple Fourier series”. *Bulletin of the American Mathematical Society* **77**, 744–745 (1971).
- [74] Charles Fefferman. “On the divergence of multiple Fourier series”. *Bulletin of the American Mathematical Society* **77**, 191–195 (1971).
- [75] Adrian W. Bowman. “An Alternative Method of Cross-Validation for the Smoothing of Density Estimates”. *Biometrika* **71**, 353–360 (1984).
- [76] F. Pedregosa, G. Varoquaux, A. Gramfort, V. Michel, B. Thirion, O. Grisel, M. Blondel, P. Prettenhofer, R. Weiss, V. Dubourg, J. Vanderplas, A. Passos, D. Cournapeau, M. Brucher, M. Perrot, and E. Duchesnay. “Scikit-learn: Machine learning in Python”. *Journal of Machine Learning Research* **12**, 2825–2830 (2011). url: <http://jmlr.org/papers/v12/pedregosa11a.html>.

## A Classical preprocessing for the Chebyshev method

### A.1 One dimension

A Lipschitz continuous function  $f$  defined on  $[-1, 1]$  has a unique expansion as a Chebyshev series,

$$f(x) = \sum_{k=0}^{\infty} \hat{c}_k T_k(x) \quad (42)$$

with coefficients

$$\hat{c}_k = \frac{2 - \delta_{k,0}}{\pi} \int_{-1}^1 \frac{dx}{\sqrt{1-x^2}} f(x) T_k(x), \quad (43)$$

where  $\delta_{k,j}$  is the Kronecker delta (see e.g. [49, Theorem 3.1]). The Chebyshev polynomials  $T_k(x)$  satisfy the orthogonality condition

$$\int_{-1}^1 \frac{dx}{\sqrt{1-x^2}} T_k(x) T_j(x) = \begin{cases} 0 & \text{if } k \neq j, \\ \frac{\pi}{2} & \text{if } k = j \neq 0, \\ \pi & \text{if } k = j = 0 \end{cases} \quad (44)$$



as well as the discrete orthogonality condition

$$\sum_{m=0}^{N-1} T_k(x_m^{(N)}) T_j(x_m^{(N)}) = \begin{cases} 0 & \text{if } k \neq j, \\ \frac{N}{2} & \text{if } k = j \neq 0, \\ N & \text{if } k = j = 0, \end{cases} \quad (45)$$

where  $x_m^{(N)} = \cos\left(\frac{\pi(2m+1)}{2N}\right)$  for  $m = 0, 1, \dots, N-1$  are the roots of the Chebyshev polynomial  $T_N(x)$ .

The analysis can be extended to complex functions. The Chebyshev series remains convergent within an ellipse in the complex plane with foci  $\pm 1$  that does not contain any poles, branch points or other singularities of  $f$  [48, Theorem 7].

For the numerical results in this paper we construct the degree- $d$  polynomial approximation Eq. (2) via interpolation. The interpolant  $f_d$  is uniquely determined by finding coefficients  $c_k$  such that  $f_d(x_m) = f(x_m)$  on a set of  $d+1$  points  $\{x_m\}_{m=0}^d$ . We choose the roots of the degree- $(d+1)$  Chebyshev polynomial as interpolation points,  $\{x_m^{(d+1)}\}_{m=0}^d$ , as this entails favorable convergence properties to the target function.

First, let us consider the interpolation error [70]. If the Chebyshev series of a function  $f$  exists, the error is bounded by  $\max_{x \in [-1, 1]} |f(x) - f_d(x)| \leq 2 \sum_{k=d+1}^{\infty} |\hat{c}_k|$  [48, Theorem 21]. Typically, the magnitude of coefficients decreases rapidly in  $k$  with a rate depending on the smoothness of  $f$ . Given a target function  $f \in C^{(d+1)}[-1, 1]$  (i.e.  $f$  is a complex function whose  $(d+1)$ -st derivative exists and is continuous on the interval  $[-1, 1]$ ), the degree- $d$  Chebyshev interpolation incurs an error

$$\varepsilon_d := \max_{x \in [-1, 1]} |f(x) - f_d(x)| = \frac{|f^{(d+1)}(\xi)|}{2^d(d+1)!} \quad (46)$$

for some  $\xi \in (-1, 1)$ . The same formula holds for truncation instead of interpolation, possibly for some other  $\xi$  [70]. If  $M$  is an upper bound for  $f^{(d+1)}$  on  $[-1, 1]$  (this exists because  $f^{(d+1)}$  is continuous on the bounded interval  $[-1, 1]$ ), then the truncation and interpolant error is upper-bounded by

$$\varepsilon_d \leq \frac{M}{2^d(d+1)!}. \quad (47)$$

The take-away message is that the Chebyshev interpolant rapidly converges to the target function if it is sufficiently smooth. The function does not need to be periodic as is the case for the Fourier expansion.

The coefficients  $c_k$  of the interpolant can be computed with the fast Fourier transform. The interpolant  $f_d$  is a Chebyshev series for a polynomial of degree at most  $d$ . Its coefficients are given exactly by applying the  $(d+1)$ -point trapezoidal rule to the integral in Eq. (43) evaluated at the  $d+1$  Chebyshev roots [48, Theorem 21]

$$c'_k = \frac{2}{d+1} \sum_{m=0}^d f_d(x_m^{(d+1)}) T_k(x_m^{(d+1)}) = \frac{2}{d+1} \sum_{m=0}^d f_d(x_m^{(d+1)}) \cos\left(k\pi \frac{2m+1}{2(d+1)}\right). \quad (48)$$

This is the discrete cosine transform, which we evaluate via the fast Fourier transform with complexity  $\mathcal{O}(d \log d)$ . The notation  $c'_k$  means we need to divide the  $k=0$  term by 2,  $c_0 = c'_0/2$  while  $c_k = c'_k$  for  $k > 0$ . The coefficients of the interpolant and infinite Chebyshev series are related via a simple formula [48, Theorem 21].

## A.2 Two and higher dimensions

To compute the 2D interpolant  $f_{d_x, d_y}(x, y)$ , Eq. (4), we match the target function at the grid points  $\left\{\left(x_m^{(d_x+1)}, y_n^{(d_y+1)}\right)\right\}_{m=0, n=0}^{d_x, d_y}$  given by the Chebyshev roots of degrees  $(d_x+1)$  and  $(d_y+1)$ . In analogy to the 1D case, the coefficients  $c_{k,l}$  of this interpolant are given by the 2D cosine transform on this grid

$$c'_{k,l} = \frac{4}{(d_x+1)(d_y+1)} \sum_{m=0}^{d_x} \sum_{n=0}^{d_y} f(x_m^{(d_x+1)}, y_n^{(d_y+1)}) \cos\left(k\pi \frac{2m+1}{2(d_x+1)}\right) \cos\left(l\pi \frac{2n+1}{2(d_y+1)}\right). \quad (49)$$

This can be evaluated with the fast Fourier transform with cost  $\mathcal{O}(d_x d_y \log(d_x d_y))$ . The notation  $c'_{k,l}$  means we need to divide the  $k=0, l=0$  terms appropriately,  $c_{k,l} = c'_{k,l}/(1+\delta_{k,0})(1+\delta_{l,0})$ .

The above procedure readily generalizes to higher dimensions. However, for high degrees or high dimensions it may become computationally more efficient to compute a low-rank approximation of  $f$  and approximate the univariate, constituent functions as Chebyshev polynomials [71].

Error bounds are more difficult to establish rigorously for the multivariate case. Ref. [72] shows that multivariate functions with a certain property display similar behavior of the maximum error as the univariate case, namely exponential convergence to the target function with increasing (total or maximal) degree.

## B Classical preprocessing for the Fourier method

Here we discuss two preprocessing steps that may be required for implementing the Fourier approach. We used those methods in Sec. 3.2. First, we describe one way to periodically extend functions which are not periodic with period 2. Second, we show how to compute coefficients in a degree- $d$  Fourier series approximation via the fast Fourier transform.

Without loss of generality consider a *bivariate* target function  $f : [0, 1]^2 \rightarrow \mathbb{C}$ , which is not periodic with period 2. To obtain a converging Fourier series, we turn the function into a periodic one. We begin by extending the domain to  $[-1, 1]^2$  by considering the function  $\tilde{f}(x, y) = f(|x|, |y|)$ . This step guarantees that the function is mirrored with respect to both coordinate axes and for both the real and imaginary part. There are no jump discontinuities in the resulting function, although the first derivative may be discontinuous. Next, we extend the domain to  $\mathbb{R}^2$  by considering the function

$$\tilde{f}(x + 2n, y + 2m) = \tilde{f}(x, y) \quad \forall n, m \in \mathbb{N}, \quad (50)$$

which is a periodic function of period 2 in both variables. Then we use this extended target function for finding Fourier series coefficients.

Next we discuss a method for computing the coefficients of a degree- $d$  trigonometric polynomial approximation to a function via interpolation and the fast Fourier transform. For simplicity let us consider the one-dimensional case, i.e. a periodic function  $f(x)$  with period 2 on the interval  $[-1, 1]$  (after applying a periodic extension if necessary). We assume  $f$  admits a Fourier series  $f(x) = \sum_{k=-\infty}^{\infty} \hat{c}_k e^{i\pi k x}$ . Its coefficients are given by

$$\hat{c}_k = \frac{1}{2} \int_{-1}^1 dx f(x) e^{-i\pi k x}. \quad (51)$$

If those coefficients are known, a valid approximation is truncation of the infinite Fourier series at degree  $d$ . If they are unknown, it is often numerically favourable to seek an interpolant  $f_d$  of the form Eq. (1) such that  $f_d(x_m) = f(x_m)$  on the set of points  $x_m = 2m/(2d+1)$  for  $m = 0, \dots, 2d$ . The coefficients of  $f_d$  are given by

$$c_k = \frac{1}{2d+1} \sum_{m=0}^{2d} f(x_m) e^{-i\frac{2\pi k m}{2d+1}}. \quad (52)$$

This follows from multiplying  $f_d(x_m)$  by  $e^{-i\pi k x_m}$ , summing over  $m$  and using discrete orthogonality of the Fourier basis functions:

$$\sum_{m=0}^{2d} f_d(x_m) e^{-i\pi k x_m} = \sum_{m=0}^{2d} \sum_{l=-d}^d c_l e^{i\pi x_m (l-k)} = \sum_{l=-d}^d c_l (2d+1) \delta_{l,k} = (2d+1) c_k. \quad (53)$$

Inserting  $x_m$  yields Eq. (52).

Note that Eq. (52) is the discrete Fourier transform of  $\{f(x_m)\}_{m=0}^{2d}$ , which can be evaluated with cost  $\mathcal{O}(d \log d)$  via the fast Fourier transform. This method generalizes to  $D$  dimensions and use of the  $D$ -dimensional fast Fourier transform with cost  $\mathcal{O}[d_1 d_2 \dots d_D \log(d_1 d_2 \dots d_D)]$ .

We do not discuss the convergence of multivariate Fourier series in general. We shall mention however that the examples presented in this paper do enjoy this property. For bivariate functions in  $L^p$ , with  $p > 1$ , and with a careful definition of the partial sums, the Fourier series converges as shown by Fefferman [73, 74].

## C Hardware experiment

### C.1 Hardware specifications

For the experimental demonstration of our state preparation algorithm, we use the H2-1 trapped-ion quantum computer. Here we summarize the relevant specifications of H2-1 at the time of the experiments performed in April and May 2024. For details, see Ref. [63]. H2-1 operates with 32 qubits implemented with  $S_{1/2}$  hyperfine clock states of  $^{171}\text{Yb}^+$  ions. The native gate set consists of single-qubit rotation gates  $\text{PhasedX}(\alpha, \beta) = R_Z(\beta) R_X(\alpha) R_Z(-\beta)$  and two-qubit gates  $\text{ZZPhase}(\theta) = e^{-i\frac{\theta}{2} Z \otimes Z}$ , parametrized by real angles  $\alpha, \beta$  and  $\theta$ . All the gate operations as well as initializations and measurements are performed in one of four gate zones, each operating in parallel. The native two-qubit gates can be applied to an arbitrary pair of qubits by shuttling ions to one of the gate zones, enabling all-to-all connectivity. Average single- and two-qubit gate infidelities are typically 0.003% and 0.2%, respectively. State preparation and measurement error is typically 0.2% on average.

## C.2 Implementation details

As discussed in Sec. 3.4, we consider the preparation of an uncorrelated and a correlated 2D Gaussian distribution  $f(x, y)$ , Eq. (39), with the same mean value  $\boldsymbol{\mu} = (\mu_x, \mu_y)^T$ , covariance matrix  $\Sigma$  parameterized by the same marginal variances  $\sigma_x^2, \sigma_y^2$  and two values of the correlation coefficient  $\rho$ . We prepare both functions on a 2D grid with  $512 \times 512$  grid points, requiring  $n_x = n_y = 9$  qubits for the spatial discretization of both axes.

For both settings, we compute the Fourier series coefficients in  $f_d(x, y)$  with degree  $d = d_x = d_y = 3$  using the following method. First, we note that both Gaussians are close to 0 at the boundary of the domain  $[0, 1]^2$ . We, thus, extend  $f(x, y)$  to  $[-1, 1]^2$  by setting the function to 0 in the extended domain. Next, assuming this function admits a Fourier series, its coefficients can be approximated via

$$\hat{c}_{k,\ell} = \frac{1}{4} \int_{[-1,1]^2} dx dy f(x, y) e^{-i\pi(xk+y\ell)} \approx \frac{1}{4} \int dx dy f(x, y) e^{i(x,y)^T \boldsymbol{\omega}} = \frac{1}{4} e^{i\boldsymbol{\mu}^T \boldsymbol{\omega} - \frac{1}{2} \boldsymbol{\omega}^T \Sigma \boldsymbol{\omega}}. \quad (54)$$

The first equality is a generalisation of Eq. (51) to the bivariate case. The second approximate equality follows from extending the integration domain to the full space  $\mathbb{R}^2$ , and setting  $\boldsymbol{\omega} = -\pi(k, \ell)^T$ . This integral is the characteristic function of the bivariate Gaussian, for which there exists an analytic formula, given by the last expression in Eq. (54). The coefficients go to 0 exponentially in  $|k|$  and  $|\ell|$ , allowing us to truncate the series at relatively small degrees  $d_x$  and  $d_y$ . We numerically observe that this method leads to a faster convergence for our specific target function compared to the method used in Sec. 3.2. This allows us to use a lower degree at a similar approximation quality. A lower degree reduces circuit depth which is crucial for the experimental implementation.

Note that in the setting of the uncorrelated Gaussian, the density  $f(x, y)$  [cf. Eq. (39)] and its Fourier series approximation  $f_d(x, y)$  factorize into a product of univariate Gaussian densities. This factorization can be exploited in the circuit construction as well. More precisely, we prepare the two univariate functions with two separate circuits as given in Fig. 4 (each with  $a = 3, n = 9$  qubits for the ancilla and main registers, respectively) and concatenate those. This considerably simplifies the circuit and reduces the gate complexity, in comparison to the full 2D state preparation circuit, cf. Fig. 5. For the uncorrelated Gaussian we obtain 123 single-qubit gates (PhasedX), 80 two-qubit gates (ZZPhase) and a depth of 42 for the full state preparation circuit. For the correlated Gaussian we obtain 266 single-qubit gates, 237 two-qubit gates and circuit depth 352.

The success probability of the algorithm is predominantly controlled by the weight  $\sum_x \sum_y |f_d(x, y)|^2$  of the prepared function in the domain  $[0, 1]^2$ , see Eq. (32). Based on a noiseless simulation of the circuit, the ideal success probabilities are given by  $p_{\text{success}} = 0.134$  and  $p_{\text{success}} = 0.139$  for the case of the correlated and uncorrelated Gaussian, respectively. The interplay between noise and circuit depth also affects the success probability. Deeper circuits increase overall noise when executed on noisy hardware, which, in general, reduces the overlap of the prepared (mixed) state with the target state  $|0\rangle^{\otimes(a_x+a_y)}$  in the ancilla registers, cf. Fig. 5. Generally, this reduces the success probability. Experimentally, we obtain a success probability  $p_{\text{success}} = 0.1299$  for the uncorrelated setting and a success probability  $p_{\text{success}} = 0.0877$  for the correlated setting.

## C.3 Kernel density estimation

Let  $\mathbf{X} = \{\mathbf{x}_1, \dots, \mathbf{x}_{N_{\text{data}}}\}$ ,  $\mathbf{x}_i \in \mathbb{R}^D$  be the observed data points in a given  $D$ -dimensional domain. Assume the data is independently drawn from a density  $f(\mathbf{x})$ . The kernel density estimate (KDE) of  $f$  based on dataset  $\mathbf{X}$  is given by

$$k_h^{\mathbf{X}}(\mathbf{x}) = \frac{1}{N_{\text{data}}} \sum_{i=1}^{N_{\text{data}}} K\left(\frac{\mathbf{x} - \mathbf{x}_i}{h}\right), \quad (55)$$

where  $K$  is the kernel, i.e. a smooth normalized function (which integrates to one over the given domain), which is often chosen to be Gaussian. The parameter  $h$  is the bandwidth. The KDE yields a smooth approximation of the density  $f$  underlying the observations  $\mathbf{x}_i$ . The bandwidth  $h$  needs to be chosen based on the competition between the smoothness of the estimate and the information it contains about the dataset. For a small bandwidth  $h$  the KDE tends to overfit the data, and in the limit of  $h \rightarrow 0$  the KDE just represents the original dataset without smoothing. For  $h \rightarrow \infty$ , on the other hand, the KDE approaches a flat distribution, which does not contain any information about the dataset  $\mathbf{X}$ .

We optimize  $h$  from the data, i.e. we do not assume access to the underlying density  $f$ , using cross validation. For this let  $\mathbf{X}_i$  be the dataset obtained from  $\mathbf{X}$  by excluding the point  $\mathbf{x}_i$ , and  $k_h^{\mathbf{X}_i}$  the corresponding KDE. The probability to observe the excluded point is given by  $k_h^{\mathbf{X}_i}(\mathbf{x}_i)$ . We want to maximize this probability, averaged over all choices of  $i$ . In practice one often works with log-probabilities. Note that, since the logarithm is a

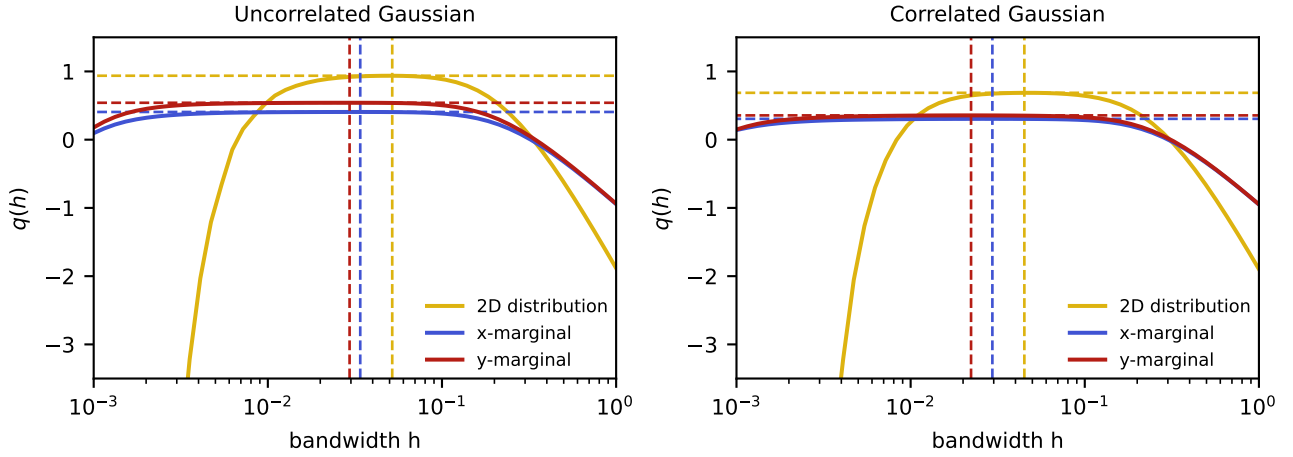


Figure 11: Cross validation of the kernel density estimates for  $f_d(x, y) = |f_d(x, y)|$  and its marginals. The results are shown for the uncorrelated and the correlated Gaussian in the left and right plots, respectively. The maximal value of the mean of log-probabilities  $q(h)$ , Eq. (56), and the corresponding bandwidth  $h$  are highlighted via vertical and horizontal dashed lines. For the uncorrelated Gaussian, the maximum of  $q(h)$  is achieved for  $\hat{h} \approx 0.052$  for the full 2D distribution, and for  $\hat{h}_x \approx 0.034$  and  $\hat{h}_y \approx 0.029$  for its marginals. For the correlated Gaussian, we obtain optimal bandwidths  $\hat{h} \approx 0.045$ ,  $\hat{h}_x \approx 0.029$  and  $\hat{h}_y \approx 0.022$ .

monotonically increasing function, maximizing  $k_h^{\mathbf{X}_i}(\mathbf{x}_i)$  is equivalent to maximizing  $\log k_h^{\mathbf{X}_i}(\mathbf{x}_i)$ . This defines our final optimizer, the mean of log-probabilities taken over  $i$ :

$$q(h) = \frac{1}{N_{\text{data}}} \sum_{i=1}^{N_{\text{data}}} \log k_h^{\mathbf{X}_i}(\mathbf{x}_i). \quad (56)$$

The optimal  $\hat{h}$  is obtained by maximizing  $q$  over  $h$ . The KDE estimate of the target density  $f$  is then given by

$$k^{\mathbf{X}} = k_{\hat{h}}^{\mathbf{X}}. \quad (57)$$

For a given  $h$ , the log-probability  $\log k_h^{\mathbf{X}_i}(\mathbf{x}_i)$  is an unbiased estimator (under the distribution of  $\mathbf{X}$ ) of the Kullback-Leibler divergence (up to a sign and a constant additive factor depending on  $f$ ) between  $f$  and  $k_h^{\mathbf{X}}$ . What this means is that  $\mathbb{E}[\log k_h^{\mathbf{X}_i}(\mathbf{x}_i)]$  asymptotically approaches  $\mathbb{E}[\int d\mathbf{x} f(\mathbf{x}) \log k_h^{\mathbf{X}}(\mathbf{x})]$  for  $N_{\text{data}} \rightarrow \infty$ , where the expectation  $\mathbb{E}[\cdot]$  is taken with respect to the distribution of  $\mathbf{X}$ , see e.g. [64, 65]. There exist alternatives to the log-probabilities which are, for example, more closely related to the mean integrated squared error (MISE) between the target density  $f$  and the estimator [65], see also [75] for a comparison of both.

In Fig. 11 we apply KDE to the data obtained from our state preparation hardware experiments, cf. Sec. C.2. To optimize  $q(h)$  [cf. Eq. (56)] we use the `scikit-learn` [76] implementations of KDE and cross validation. We first consider the datasets of the full 2D state preparation circuit. The dataset  $\mathbf{X}$  is given by the two-dimensional points  $\mathbf{x}_i = (x_i, y_i)$  (as represented via bitstrings, see Sec. 2.1) measured at the output of our state preparation algorithm, see Appendix C.1 and C.2. In case of the uncorrelated Gaussian, we have  $N_{\text{data}} = 2598$  data points, for the correlated one we have  $N_{\text{data}} = 1754$ . The yellow solid curves in both plots of Fig. 11 show  $q$  as a function of the bandwidth  $h$ , for both settings. We obtain optimal bandwidths (vertical yellow dashed lines) of  $\hat{h} \approx 0.052$  (uncorrelated Gaussian) and  $\hat{h} \approx 0.045$  (correlated Gaussian). We repeat the same procedure for the marginals. The blue and red solid curves in Fig. 11 show  $q(h)$  when we use  $\mathbf{X} = \{x_1, \dots, x_{N_{\text{data}}}\}$  (the x-marginal) and  $\mathbf{X} = \{y_1, \dots, y_{N_{\text{data}}}\}$  (the y-marginal), respectively. Optimal marginal KDE are obtained for bandwidths  $\hat{h}_x \approx 0.034$ ,  $\hat{h}_y \approx 0.029$  for the setting of the uncorrelated Gaussian, and  $\hat{h}_x \approx 0.029$ ,  $\hat{h}_y \approx 0.022$  for the correlated Gaussian, as indicated by the vertical dashed blue and red lines in the plots, respectively.